Localized light orbitals: Basis states for three-dimensional photonic crystal microscale circuits

Hiroyuki Takeda, Alongkarn Chutinan, and Sajeev John
Department of Physics, University of Toronto, 60 St. George St., Toronto, Ontario, Canada M5S 1A7
(Received 16 June 2006; revised manuscript received 8 September 2006; published 20 November 2006)

We demonstrate the utility of three-dimensional (3D) optical Wannier functions (WF's) for quantitative description of electromagnetic wave localization and propagation in 3D photonic band gap (PBG) microcircuits. Using these localized "optical orbitals" we reconstruct electromagnetic waveguiding in bulk two-dimensional (2D) and 3D PBG materials, 2D-3D PBG heterostructures composed of 3D PBG structures inserted with 2D microchip layers, and 2D membrane photonic crystals. In 3D photonic crystal circuits, the expansion of electromagnetic fields with typically less than 20 maximally localized WF's (MLWF's) simplifies the calculation of electromagnetic phenomena of spectral bandwidth surrounding the PBG and improves computational efficiency, compared to the plane wave expansion and the finite-difference time-domain methods. The MLWF's are defined by a unitary transformation on the extended Bloch mode basis, chosen to minimize a wave function delocalization functional, while retaining symmetries of the underlying Bloch modes. We introduce an effective approach to constructing modified MLWF's in 3D architectures involving surface polarization charges and electromagnetic field discontinuities. These modified optical orbitals are also corrected for Gibbs phenomena arising near sharp dielectric interfaces. We demonstrate the accuracy of our localized light orbital method for recapturing TM and TE modes in idealized 2D photonic crystals and mixed polarization waveguide modes in 3D architectures.

DOI: 10.1103/PhysRevB.74.195116 PACS number(s): 42.70.Qs, 42.25.Bs, 71.15.−m

I. INTRODUCTION

Photonic band gap (PBG) materials[1,2] are engineered dielectric microstructures in which light can be localized.[1,3] These complex, three-dimensional (3D) scattering, microstructures enable unprecedented forms of optical waveguiding.[4–6] These "semiconductors of light" enable large scale integration of optical components within an optical microchip. New and powerful computational methods are required to describe electromagnetic confinement and flow within these complex architectures. Since light localization is the fundamental physical phenomenon associated with PBG materials, it is natural to describe electromagnetic effects in the PBG using localized optical basis functions.[7–13] These localized Wannier functions (WF's)[14] are the electromagnetic analogues of electronic orbitals in atomic physics. Using such localized optical basis states, it is possible to efficiently and accurately map electromagnetic phenomena in optical microcircuits to "tight-binding" wave equations,[15] analogous to those used to describe confined electrons in solids.

PBG structures enable unconventional guiding of light in air waveguides and dense integration of microscopic optical components,[4,16–20] into an optical microchip. In conventional optical circuits, diffraction and scattering losses may become prohibitive at sharp waveguide bends and in the presence of surface roughness. The PBG, on the other hand, eliminates such leakages of light at a fundamental level. The optical WF method provides an efficient and accurate description of these effects by selecting the electromagnetic modes relevant to the PBG spectral range prior to simulating light flow through the microcircuit. Unlike previous work that has focused on idealized two-dimensional (2D) photonic crystals (PC's),[9–13] we demonstrate that a localized optical orbital basis can be successfully applied to experimentally relevant 3D microstructures where the full vector nature of the electromagnetic field must be considered. Unlike earlier work on 2D TM optical modes, our 3D localized light orbitals must account for modified surface polarization charges and vector-field discontinuities that occur near defects in the photonic crystal.

In earlier theoretical analysis of the PC's, computational methods such as the plane wave expansion (PWE) and the finite-difference time-domain (FDTD) method have been employed. While the PWE method constructs electromagnetic wave effects starting from a basis of extended plane waves,[21,22] the FDTD method reconstructs the same phenomena starting from a point localized basis of delta functions. This leads to a discretization of time and space in Maxwell's equations.[23] In the PC's without defects, photonic band structures can be calculated easily by the PWE method whereas for point-defect and guided modes, the supercell PWE technique is utilized. In the simulation of light propagation in the PC circuits, the FDTD method is preferred. In idealized 2D PC's with a small number of optical circuit elements, the PWE and the FDTD methods are adequate. However, in large scale 3D PC circuits, these methods become prohibitively time consuming. In the PWE method applied to a supercell, typically many thousands of the plane waves must be taken. Likewise the FDTD method, consisting of a discrete lattice of points with at least 10 points per direction in a unit cell of the PC, requires many thousands of basis (delta) functions in a 3D PC unit cell. Both the PWE and the FDTD methods utilize an overcomplete basis for the relevant spectral range of typical 3D circuit paths in a large scale PBG microchip. Moreover, in the FDTD method, even for small circuit paths, high accuracies cannot be obtained near the frequencies of photonic band edges because of low group velocities for light pulse propagation.[16]

In view of recent developments in the design[24,25] and microfabrication[26] of broad bandwidth optical circuit architecture in 3D PBG materials, it is timely to implement a

fundamentally new and efficient algorithm for simulating light flow in these systems. The basic simplification arises from recognizing that both the PWE and the FDTD methods provide an unnecessarily broadband description of wave propagation, covering not only the PBG spectrum but also many, many photonic bands above and below the region of interest. The localized optical orbital basis, on the other hand, focuses attention on the relevant spectral region for light propagation in microcircuit paths spectrally located within or near the PBG. This enables an accurate description of electromagnetic effects in 3D with typically less than 20 localized optical basis functions per unit cell.

Recently, the successful application of the optical WF method to 2D PC circuits for TM polarized waves has been reported.[12] In this important work,[12] the results of the FDTD method were accurately recaptured by representing optical fields as an expansion in only six maximally localized WF's (MLWF's). In this case, the electric field vector is always normal to the plane of periodicity and the vector wave equation can be reduced to a scalar one. In 3D PC's, however, we must consider vector equations. Accordingly, the 3D optical WF's are vector functions. We construct 3D MLWF's starting with magnetic fields, and then use Maxwell's equations to recapture the electric fields. In the calculation of light propagation in the 3D PBG circuits, we consider the electric-field wave equation derived from Maxwell's equations. We then expand the electric fields in terms of the MLWF's to reduce the wave equation to sparse matrix equations (tight-binding model) involving a small number of expansion coefficients of the 3D optical Wannier orbitals. We demonstrate that the optical WF method applied to the 3D PC circuits simplifies the computational task, compared to PWE and FDTD methods.

We begin by reviewing the application of 2D optical WF method to TM and TE modes in 2D PBG structures. We discuss the modification in representation required for accurate description of the 2D TE mode in which electric field discontinuities may appear as a result of surface polarization charges. We then introduce and apply the 3D optical WF method to bulk 3D PBG structures, 2D-3D PBG heterostructures,[5,6] and 2D membrane PC's. Although in idealized 2D PBG structures light is assumed not to leak in the direction perpendicular to 2D planes, in reality we cannot neglect such leakage. 2D-3D PBG heterostructures containing 2D microchip layers sandwiched between 3D PBG cladding layers were introduced to eliminate such leakages of light in the third dimension.[5,6] On the other hand, 2D membrane PC's are composed of periodic air holes in slabs of finite thickness. Here, only light that satisfies the condition of total internal reflection is confined strictly to propagate within the membrane.

II. WANNIER FUNCTIONS IN GENERAL BULK PBG CRYSTALS

A. Periodic dielectrics

In this section, we describe the general method of constructing WF's in bulk 2D and 3D PBG structures, starting from the magnetic-field Maxwell wave equation:

$$\nabla \times [\epsilon_p^{-1}(\mathbf{r}) \nabla \times \mathbf{H}(\mathbf{r})] = \frac{\omega^2}{c^2}\mathbf{H}(\mathbf{r}), \tag{1}$$

where $\epsilon_p(\mathbf{r})$ is the dielectric index of the periodic PBG structure, $\epsilon_p(\mathbf{r})=\epsilon_p(\mathbf{r}+\mathbf{R})$ and $\mathbf{R}$ is the lattice vector. A Bloch function of the magnetic field is expressed as

$$\mathbf{H}^{(0)}_{n\mathbf{k}}(\mathbf{r}) = e^{i\mathbf{k}\cdot\mathbf{r}}\mathbf{h}^{(0)}_{n\mathbf{k}}(\mathbf{r}), \tag{2}$$

where the periodic part of the Bloch function is defined as follows:

$$\mathbf{h}^{(0)}_{n\mathbf{k}}(\mathbf{r}) = \sum_{\mathbf{G}} \mathbf{h}^{(0)}_{n\mathbf{k}}(\mathbf{G}) e^{i\mathbf{G}\cdot\mathbf{r}}, \tag{3}$$

where $\mathbf{G}$ is the reciprocal lattice vector. n and $\mathbf{k}$ indicate the photonic band index and the wave vector, respectively. The superscript (0) is included here to indicate that these functions are true solutions of the wave equation of Eq. (1). In what follows, we will construct new basis functions $\mathbf{H}_{n\mathbf{k}}(\mathbf{r})$ that are linear combinations of $\mathbf{H}^{(0)}_{m\mathbf{k}}(\mathbf{r})$ over a set of bands $m=1,\ldots,N$, but not necessarily solutions (1). The solutions, $\mathbf{H}^{(0)}_{n\mathbf{k}}(\mathbf{r})$ satisfy an orthogonality,

$$\int_V d^d\mathbf{r}\mathbf{H}^{(0)*}_{n\mathbf{k}}(\mathbf{r}) \cdot \mathbf{H}^{(0)}_{n'\mathbf{k}'}(\mathbf{r}) = \frac{(2\pi)^d}{v}\delta_{nn'}\delta(\mathbf{k}-\mathbf{k}'). \tag{4}$$

Here $d(=2,3)$ is the dimension, integration is over the entire d-dimensional volume V, and v is the volume of the 2D (or 3D) unit cell.

In constructing maximally localized Wanneir orbitals, it is useful to consider linear combinations of Bloch functions of the form $\mathbf{H}_{n\mathbf{k}}(\mathbf{r})=\Sigma_{m=1}^{N} U^{(\mathbf{k})}_{mn}\mathbf{H}^{(0)}_{m\mathbf{k}}(\mathbf{r})$, where $U^{(\mathbf{k})}_{mn}$ is an arbitrary unitary matrix defined for each $\mathbf{k}$ point. This unitary transformation preserves the orthogonality relation Eq. (4). A general WF of the magnetic field $\mathbf{W}^{(\mathbf{H})}_{n\mathbf{R}}(\mathbf{r})$ $(n=1,2,\ldots,N)$, centered at position $\mathbf{R}$, is then defined as follows:

$$\mathbf{W}^{(\mathbf{H})}_{n\mathbf{R}}(\mathbf{r}) = \frac{v}{(2\pi)^d}\int_{\mathrm{BZ}} d^d\mathbf{k} e^{-i\mathbf{k}\cdot\mathbf{R}}\mathbf{H}_{n\mathbf{k}}(\mathbf{r}), \tag{5}$$

$$\mathbf{H}_{n\mathbf{k}}(\mathbf{r}) = \sum_{\mathbf{R}} e^{i\mathbf{k}\cdot\mathbf{R}}\mathbf{W}^{(\mathbf{H})}_{n\mathbf{R}}(\mathbf{r}), \tag{6}$$

where the latter sum is over the set of all direct lattice vectors $\mathbf{R}$.

In practice, the integral in Eq. (5) is treated as the sum of the Bloch functions at discrete $\mathbf{k}$ points over the first BZ. $\mathbf{W}^{(\mathbf{H})}_{n\mathbf{R}}(\mathbf{r})$ satisfies the orthogonality relation,

$$\langle \mathbf{W}^{(\mathbf{H})}_{n\mathbf{R}} | \mathbf{W}^{(\mathbf{H})}_{n'\mathbf{R}'} \rangle \equiv \int_V d^d\mathbf{r}\mathbf{W}^{(\mathbf{H})*}_{n\mathbf{R}}(\mathbf{r}) \cdot \mathbf{W}^{(\mathbf{H})}_{n'\mathbf{R}'}(\mathbf{r}) = \delta_{nn'}\delta_{\mathbf{R}\mathbf{R}'}. \tag{7}$$

Since the operator $\nabla \times \epsilon_p^{-1}(\mathbf{r}) \nabla \times$ in Eq. (1) is Hermitian, we can impose the symmetries $\mathbf{H}_{n\mathbf{k}}(\mathbf{r})=\mathbf{H}^{*}_{n-\mathbf{k}}(\mathbf{r})$ and $U^{(\mathbf{k})}_{mn} = U^{(-\mathbf{k})*}_{mn}$. In this case, the WF's of the magnetic fields can be chosen real. We now consider an expansion of the magnetic field in Eq. (1) in the basis of WF's defined by Eq. (6),

$$\mathbf{H}(\mathbf{r}) = \sum_{n=1}^{N} \sum_{\mathbf{R}} c_n e^{i\mathbf{k}\cdot\mathbf{R}} \mathbf{W}_{n\mathbf{R}}^{(\mathbf{H})}(\mathbf{r}), \tag{8}$$

where c_n are undetermined coefficients. By substituting Eq. (8) into Eq. (1) and using the orthogonality of the WF's, the following eigenvalue equation is obtained:

$$\sum_{n'=1}^{N} \left(\sum_{\mathbf{R}'} e^{i\mathbf{k}\cdot\mathbf{R}'} A_{\mathbf{0R}'}^{nn'} \right) c_{n'} = \frac{\omega^2}{c^2} c_n, \tag{9}$$

where the tight-binding matrix element is defined as

$$A_{\mathbf{RR}'}^{nn'} \equiv \langle \mathbf{W}_{n\mathbf{R}}^{(\mathbf{H})} | \nabla \times \epsilon_p^{-1} \nabla \times | \mathbf{W}_{n'\mathbf{R}'}^{(\mathbf{H})} \rangle = \frac{v}{(2\pi)^d} \int_{\mathrm{BZ}} d^d\mathbf{k} e^{i\mathbf{k}\cdot(\mathbf{R}-\mathbf{R}')} \sum_{m=1}^{N} U_{nm}^{(\mathbf{k})\dagger} \left(\frac{\omega_{m\mathbf{k}}}{c} \right)^2 U_{mn'}^{(\mathbf{k})}. \tag{10}$$

By solving the eigenvalue matrix in Eq. (9), the photonic band structure is reproduced in the WF basis. When the WF's are very well localized, $A_{\mathbf{RR}'}^{nn'}$ decays rapidly with increasing $|\mathbf{R}-\mathbf{R}'|$, and we can take a small number of the lattice vectors $\mathbf{R}$ in Eq. (9). Typically, this corresponds to retaining nonzero contributions from matrix elements $A_{\mathbf{RR}'}^{nn'}$ such that $|\mathbf{R}-\mathbf{R}'| \leqslant 4a$ where a is the photonic crystal lattice constant.

The magnetic WF's can be used to obtain electric field orbitals using the Maxwell equation. The electric field Bloch function $\mathbf{E}_{n\mathbf{k}}^{(0)}(\mathbf{r}) = i(c/\omega_{n\mathbf{k}})\epsilon_p^{-1}(\mathbf{r}) \nabla \times \mathbf{H}_{n\mathbf{k}}^{(0)}(\mathbf{r})$ satisfies the orthogonality relation,

$$\int_V d^d\mathbf{r} \epsilon_p(\mathbf{r}) \mathbf{E}_{n\mathbf{k}}^{(0)*}(\mathbf{r}) \cdot \mathbf{E}_{n'\mathbf{k}'}^{(0)}(\mathbf{r}) = \frac{(2\pi)^d}{v} \delta_{nn'} \delta(\mathbf{k}-\mathbf{k}'). \tag{11}$$

Defining $\mathbf{E}_{n\mathbf{k}}(\mathbf{r}) = \Sigma_{m=1}^{N} U_{mn}^{(\mathbf{k})} \mathbf{E}_{m\mathbf{k}}^{(0)}(\mathbf{r})$, the WF's of the electric fields $\mathbf{W}_{n\mathbf{R}}^{(\mathbf{E})}(\mathbf{r})$ are given by

$$\mathbf{W}_{n\mathbf{R}}^{(\mathbf{E})}(\mathbf{r}) = \frac{v}{(2\pi)^d} \int_{\mathrm{BZ}} d^d\mathbf{k} e^{-i\mathbf{k}\cdot\mathbf{R}} \mathbf{E}_{n\mathbf{k}}(\mathbf{r}) \tag{12}$$

and satisfy the orthogonality relation,

$$\langle \mathbf{W}_{n\mathbf{R}}^{(\mathbf{E})} | \epsilon_p | \mathbf{W}_{n'\mathbf{R}'}^{(\mathbf{E})} \rangle \equiv \int_V d^d\mathbf{r} \epsilon_p(\mathbf{r}) \mathbf{W}_{n\mathbf{R}}^{(\mathbf{E})*}(\mathbf{r}) \cdot \mathbf{W}_{n'\mathbf{R}'}^{(\mathbf{E})}(\mathbf{r}) = \delta_{nn'} \delta_{\mathbf{RR}'}. \tag{13}$$

Since $\mathbf{H}_{n\mathbf{k}}(\mathbf{r}) = \mathbf{H}_{n-\mathbf{k}}^{*}(\mathbf{r})$ and $U_{mn}^{(\mathbf{k})} = U_{mn}^{(-\mathbf{k})*}$, it follows that $\mathbf{E}_{n\mathbf{k}}(\mathbf{r}) = -\mathbf{E}_{n-\mathbf{k}}^{*}(\mathbf{r})$ and the electric field WF's are pure imaginary. Spatial profiles of the WF's are calculated from the sum of Bloch functions over $\mathbf{k}$ points spanning the first BZ. Since the Bloch functions are represented by a Fourier series expansion of reciprocal lattice vectors, their distributions can easily be calculated by a fast Fourier transformation. In Sec. II C, we discuss the choice of unitary matrices $U_{mn}^{(\mathbf{k})}$ that provides maximal localization of these optical orbitals. We first describe a key modification of the Wannier function that arises from their vector nature and which is central to their ability to describe electromagnetic effects in the presence of defects in the otherwise periodic photonic crystal.

B. Defects and surface polarization charge

In the presence of a dielectric defect $\delta\epsilon(\mathbf{r})$ over and above the periodic dielectric functions, we start with the electric-field Maxwell wave equation,

$$\nabla \times [\nabla \times \mathbf{E}(\mathbf{r})] = \frac{\omega^2}{c^2} \epsilon(\mathbf{r}) \mathbf{E}(\mathbf{r}), \tag{14}$$

$$\nabla \cdot [\epsilon(\mathbf{r}) \mathbf{E}(\mathbf{r})] = 0, \tag{15}$$

where $\epsilon(\mathbf{r}) = \epsilon_p(\mathbf{r}) + \delta\epsilon(\mathbf{r})$. In scalar wave WF theory,[12,13,27,28] the electric field near such a defect is expanded in the basis of unperturbed functions $\mathbf{W}_{n\mathbf{R}}^{(\mathbf{E})}(\mathbf{r})$. However, for a general 3D electromagnetic vector field, the modified distribution of surface polarization charges cannot be represented by WF's constructed to describe the original surface charge distribution: $\nabla \cdot [\epsilon_p(\mathbf{r}) \mathbf{W}_{n\mathbf{R}}^{(\mathbf{E})}(\mathbf{r})] = 0$. In general, the electric field is represented by scalar and vector potentials. The electric field is expanded in the basis of localized scalar and vector potentials $\phi_{n\mathbf{R}}(\mathbf{r})$ and $\mathbf{A}_{n\mathbf{R}}(\mathbf{r})$, respectively,

$$\mathbf{E}(\mathbf{r}) = \sum_{n\mathbf{R}} E_{n\mathbf{R}} \left(-\nabla \phi_{n\mathbf{R}}(\mathbf{r}) + i \frac{\omega}{c} \mathbf{A}_{n\mathbf{R}}(\mathbf{r}) \right), \tag{16}$$

where $E_{n\mathbf{R}}$ is the expansion coefficient. We choose a gauge: $\nabla \cdot [\epsilon_p(\mathbf{r}) \mathbf{A}_{n\mathbf{R}}(\mathbf{r})] = 0$, and then, take $i(\omega/c)\mathbf{A}_{n\mathbf{R}}(\mathbf{r}) = \mathbf{W}_{n\mathbf{R}}^{(\mathbf{E})}(\mathbf{r})$ because of $\nabla \cdot [\epsilon_p(\mathbf{r}) \mathbf{W}_{n\mathbf{R}}^{(\mathbf{E})}(\mathbf{r})] = 0$. In order to represent the induced polarization charge of the defect and enforce the condition that the defect does not introduce any free charge carriers, we write

$$\mathbf{E}(\mathbf{r}) = \sum_{n\mathbf{R}} E_{n\mathbf{R}} \tilde{\mathbf{W}}_{n\mathbf{R}}^{(\mathbf{E})}(\mathbf{r}), \tag{17}$$

where $\tilde{\mathbf{W}}_{n\mathbf{R}}^{(\mathbf{E})}(\mathbf{r}) = \mathbf{W}_{n\mathbf{R}}^{(\mathbf{E})}(\mathbf{r}) - \nabla \phi_{n\mathbf{R}}(\mathbf{r})$. $\phi_{n\mathbf{R}}(\mathbf{r})$ satisfies the Poisson equation,

$$\nabla \cdot [\epsilon(\mathbf{r}) \nabla \phi_{n\mathbf{R}}(\mathbf{r})] = \nabla \cdot [\delta\epsilon(\mathbf{r}) \mathbf{W}_{n\mathbf{R}}^{(\mathbf{E})}(\mathbf{r})]. \tag{18}$$

The right-hand side in this equation corresponds to a polarization charge density created by $\delta\epsilon(\mathbf{r})$. With the modified expansion of $\mathbf{E}(\mathbf{r})$, it is straightforward to verify that the electric field satisfies the divergence condition (15) including defects, even though $\mathbf{W}_{n\mathbf{R}}^{(\mathbf{E})}(\mathbf{r})$ obey the divergence condition for the purely periodic PC. We refer to $\mathbf{W}_{n\mathbf{R}}^{(\mathbf{E})}(\mathbf{r})$ and $\tilde{\mathbf{W}}_{n\mathbf{R}}^{(\mathbf{E})}(\mathbf{r})$ as the unmodified and modified optical WF's, respectively. By substituting Eq. (17) into Eq. (14) and using the orthogonality of the WF's, we obtain the "tight-binding" matrix equation,

$$\sum_{n'\mathbf{R}'} A_{\mathbf{RR}'}^{nn'} E_{n'\mathbf{R}'} = \frac{\omega^2}{c^2} \sum_{n'\mathbf{R}'} (\delta_{nn'}\delta_{\mathbf{RR}'} + D_{\mathbf{RR}'}^{nn'} + F_{\mathbf{RR}'}^{nn'}) E_{n'\mathbf{R}'}, \tag{19}$$

where

$$A_{\mathbf{RR}'}^{nn'} \equiv \langle \mathbf{W}_{n\mathbf{R}}^{(\mathbf{E})} | \nabla \times \nabla \times | \mathbf{W}_{n'\mathbf{R}'}^{(\mathbf{E})} \rangle = \frac{v}{(2\pi)^d} \int_{\mathrm{BZ}} d^d\mathbf{k} e^{i\mathbf{k}\cdot(\mathbf{R}-\mathbf{R}')} \sum_{m=1}^{N} U_{nm}^{(\mathbf{k})\dagger} \left(\frac{\omega_{m\mathbf{k}}}{c} \right)^2 U_{mn'}^{(\mathbf{k})}, \tag{20}$$

$$D_{\mathbf{RR}'}^{nn'} \equiv \langle \mathbf{W}_{n\mathbf{R}}^{(\mathbf{E})} | \delta\epsilon | \mathbf{W}_{n'\mathbf{R}'}^{(\mathbf{E})} \rangle = \int_V d^d\mathbf{r}\, \delta\epsilon(\mathbf{r}) \mathbf{W}_{n\mathbf{R}}^{(\mathbf{E})*}(\mathbf{r}) \cdot \mathbf{W}_{n'\mathbf{R}'}^{(\mathbf{E})}(\mathbf{r}), \tag{21}$$

and

$$F_{\mathbf{RR}'}^{nn'} \equiv -\langle \mathbf{W}_{n\mathbf{R}}^{(\mathbf{E})} | \epsilon_p + \delta\epsilon | \nabla \phi_{n'\mathbf{R}'} \rangle = -\langle \mathbf{W}_{n\mathbf{R}}^{(\mathbf{E})} | \delta\epsilon | \nabla \phi_{n'\mathbf{R}'} \rangle = -\int_V d^d\mathbf{r}\, \delta\epsilon(\mathbf{r}) \mathbf{W}_{n\mathbf{R}}^{(\mathbf{E})*}(\mathbf{r}) \cdot \nabla \phi_{n'\mathbf{R}'}(\mathbf{r}). \tag{22}$$

$A_{\mathbf{RR}'}^{nn'}$ is the tight-binding "hopping" matrix element, and $D_{\mathbf{RR}'}^{nn'}$ and $F_{\mathbf{RR}'}^{nn'}$ are the overlap matrix elements of the WF's with the defect structures. In Eq. (22), we used $\langle \mathbf{W}_{n\mathbf{R}}^{(\mathbf{E})} | \epsilon_p | \nabla \phi_{n'\mathbf{R}'} \rangle = -\langle \nabla \cdot (\epsilon_p \mathbf{W}_{n\mathbf{R}}^{(\mathbf{E})}) | \phi_{n'\mathbf{R}'} \rangle = 0$. When these matrix elements decay rapidly with increasing $|\mathbf{R}-\mathbf{R}'|$, the matrix equation becomes sparse. While it is clear that $A_{\mathbf{RR}'}^{nn'}$ and $D_{\mathbf{RR}'}^{nn'}$ are Hermitian, it can be shown that $F_{\mathbf{RR}'}^{nn'}$ is also Hermitian: $F_{\mathbf{RR}'}^{nn'} = -\langle \mathbf{W}_{n\mathbf{R}}^{(\mathbf{E})} | \delta\epsilon | \nabla \phi_{n'\mathbf{R}'} \rangle = \langle \nabla \cdot (\delta\epsilon \mathbf{W}_{n\mathbf{R}}^{(\mathbf{E})}) | \phi_{n'\mathbf{R}'} \rangle = \langle \nabla \cdot [(\epsilon_p + \delta\epsilon) \nabla \phi_{n\mathbf{R}}] | \phi_{n'\mathbf{R}'} \rangle = -\langle \nabla \phi_{n\mathbf{R}} | \epsilon_p + \delta\epsilon | \nabla \phi_{n'\mathbf{R}'} \rangle$. The tight-binding wave equation (19) enables us to calculate electromagnetic flow through waveguides and point-defect modes as well as transmission and reflection of light within complex 3D PBG circuit paths.[12,29]

According to Eq. (22), we require distributions of the scalar potential $\phi_{n\mathbf{R}}(\mathbf{r})$ only with defect regions where $\delta\epsilon(\mathbf{r}) \neq 0$. For simplicity, we consider a hypothetical periodic dielectric $\tilde{\epsilon}(\mathbf{r}) \equiv \epsilon_p(\mathbf{r}) + \delta\epsilon_p(\mathbf{r})$, $\delta\epsilon_p(\mathbf{r}) \equiv \Sigma_{\mathbf{R}} \delta\epsilon(\mathbf{r}+\mathbf{R})$ for the purpose of solving the Poisson equation (18),

$$\nabla \cdot [\tilde{\epsilon}(\mathbf{r}) \nabla \phi_{n\mathbf{R}}(\mathbf{r})] = \nabla \cdot [\delta\epsilon_p(\mathbf{r}) \mathbf{W}_{n\mathbf{R}}^{(\mathbf{E})}(\mathbf{r})], \tag{23}$$

$\delta\epsilon_p(\mathbf{r}) \mathbf{W}_{n\mathbf{R}}^{(\mathbf{E})}(\mathbf{r})$ exhibits abrupt discontinuous changes at the surface of defects. When expanding such discontinuous functions using a small number of sinusoidal terms, care must be taken to correct for the Gibbs phenomenon.[30] Taking the divergence of such spurious oscillations introduces spurious polarization charges that undermine high accuracy. In our calculations, we eliminate the Gibbs phenomenon by using the smoothing called the σ approximation. Details of solving the Poisson equation are discussed in Appendix A.

An alternative formulation of the tight-binding wave equation follows from considering matrix elements of magnetic field Wannier functions.[31] Expanding the magnetic field $\mathbf{H}(\mathbf{r})$ in the basis of WF's as

$$\mathbf{H}(\mathbf{r}) = \sum_{n\mathbf{R}} H_{n\mathbf{R}} \mathbf{W}_{n\mathbf{R}}^{(\mathbf{H})}(\mathbf{r}), \tag{24}$$

using expansion coefficients $H_{n\mathbf{R}}$, the magnetic field satisfies

$$\nabla \cdot \mathbf{H}(\mathbf{r}) = 0, \tag{25}$$

regardless of defect structures. This follows from $\nabla \cdot \mathbf{W}_{n\mathbf{R}}^{(\mathbf{H})}(\mathbf{r}) = 0$. In the presence of defects, the magnetic-field Maxwell wave equation is

$$\nabla \times [\epsilon_p^{-1}(\mathbf{r}) \nabla \times \mathbf{H}(\mathbf{r})] + \nabla \times [\delta\epsilon^{-1}(\mathbf{r}) \nabla \times \mathbf{H}(\mathbf{r})] = \frac{\omega^2}{c^2} \mathbf{H}(\mathbf{r}), \tag{26}$$

where $\delta\epsilon^{-1}(\mathbf{r}) = [\epsilon_p(\mathbf{r}) + \delta\epsilon(\mathbf{r})]^{-1} - \epsilon_p^{-1}(\mathbf{r})$. By substituting Eq. (24) into Eq. (26) and using the orthogonality of the WF's, we obtain the matrix equation

$$\sum_{n'\mathbf{R}'} (A_{\mathbf{RR}'}^{nn'} + B_{\mathbf{RR}'}^{nn'}) H_{n'\mathbf{R}'} = \frac{\omega^2}{c^2} H_{n\mathbf{R}}, \tag{27}$$

where

$$A_{\mathbf{RR}'}^{nn'} \equiv \langle \mathbf{W}_{n\mathbf{R}}^{(\mathbf{H})} | \nabla \times \epsilon_p^{-1} \nabla \times | \mathbf{W}_{n'\mathbf{R}'}^{(\mathbf{H})} \rangle = \frac{v}{(2\pi)^d} \int_{\mathrm{BZ}} d^d\mathbf{k} e^{i\mathbf{k}\cdot(\mathbf{R}-\mathbf{R}')} \sum_{m=1}^{N} U_{nm}^{(\mathbf{k})\dagger} \left(\frac{\omega_{m\mathbf{k}}}{c} \right)^2 U_{mn'}^{(\mathbf{k})} \tag{28}$$

and

$$B_{\mathbf{RR}'}^{nn'} \equiv \langle \mathbf{W}_{n\mathbf{R}}^{(\mathbf{H})} | \nabla \times \delta\epsilon^{-1} \nabla \times | \mathbf{W}_{n'\mathbf{R}'}^{(\mathbf{H})} \rangle = \int_V d^d\mathbf{r}\, \delta\epsilon^{-1}(\mathbf{r}) [\nabla \times \mathbf{W}_{n\mathbf{R}}^{(\mathbf{H})}(\mathbf{r})]^* \cdot [\nabla \times \mathbf{W}_{n'\mathbf{R}'}^{(\mathbf{H})}(\mathbf{r})]. \tag{29}$$

Although this matrix equation is equivalent to the electric field formulation, accurate convergence is more difficult to achieve. In Sec. IV A, we discuss the relative efficiency of the electric and magnetic-field optical WF methods.

C. Maximally localized optical orbitals

A variety of different localized light orbitals can be constructed depending on the choice of unitary transformation $U_{mn}^{(\mathbf{k})}$. In the context of electronics, a method of constructing MLWF's has been developed.[27,28] Following this procedure, we construct the maximally localized magnetic field WF's. These maximally localized orbitals are defined by the unitary transformation that minimizes the spread functional,

$$\Omega = \sum_{n=1}^{N} [\langle r^2 \rangle_n - (\bar{\mathbf{r}}_n)^2], \tag{30}$$

where

$$\bar{\mathbf{r}}_n = \langle \mathbf{W}_{n0}^{(\mathbf{H})} | \mathbf{r} | \mathbf{W}_{n0}^{(\mathbf{H})} \rangle \tag{31}$$

and

$$\langle r^2\rangle_n = \langle \mathbf{W}_{\mathbf{n0}}^{(\mathbf{H})}|\mathbf{r}^2|\mathbf{W}_{n0}^{(\mathbf{H})}\rangle. \tag{32}$$

We can decompose Ω into two terms $\Omega=\Omega_I+\tilde{\Omega}$, where

$$\Omega_I = \sum_{n=1}^{N}\left(\langle r^2\rangle_n - \sum_{m\mathbf{R}}|\langle \mathbf{W}_{m\mathbf{R}}^{(\mathbf{H})}|\mathbf{r}|\mathbf{W}_{n0}^{(\mathbf{H})}\rangle|^2\right) \tag{33}$$

is invariant under the band-mixing unitary transformation and

$$\tilde{\Omega} = \sum_{n=1}^{N}\sum_{m\mathbf{R}\neq n0}|\langle \mathbf{W}_{m\mathbf{R}}^{(\mathbf{H})}|\mathbf{r}|\mathbf{W}_{\mathbf{n0}}^{(\mathbf{H})}\rangle|^2 \tag{34}$$

is the remainder. When minimizing the total spread functional with respect to the parameters $U_{mn}^{(\mathbf{k})}$, we need to only consider $\tilde{\Omega}$. In what follows, the dependence of Ω on the parameters $U_{mn}^{(\mathbf{k})}$ is implicit through the definition: $|\mathbf{h}_{n\mathbf{k}}\rangle = \Sigma_{m=1}^{N} U_{mn}^{(\mathbf{k})}|\mathbf{h}_{m\mathbf{k}}^{(0)}\rangle$, where $|\mathbf{h}_{m\mathbf{k}}^{(0)}\rangle$ is the ket vector associated with the periodic part of the magnetic Bloch function [see Eq. (3)]. Matrix elements of the position operator can be expressed as follows:

$$\langle \mathbf{W}_{m\mathbf{R}}^{(\mathbf{H})}|\mathbf{r}|\mathbf{W}_{n0}^{(\mathbf{H})}\rangle = i\frac{v}{(2\pi)^d}\int_{\mathrm{BZ}} d^d\mathbf{k}e^{i\mathbf{k}\cdot\mathbf{R}}\langle \mathbf{h}_{m\mathbf{k}}|\nabla_{\mathbf{k}}|\mathbf{h}_{n\mathbf{k}}\rangle, \tag{35}$$

$$\langle \mathbf{W}_{m\mathbf{R}}^{(\mathbf{H})}|\mathbf{r}^2|\mathbf{W}_{n0}^{(\mathbf{H})}\rangle = -\frac{v}{(2\pi)^d}\int_{\mathrm{BZ}} d^d\mathbf{k}e^{i\mathbf{k}\cdot\mathbf{R}}\langle \mathbf{h}_{m\mathbf{k}}|\nabla_{\mathbf{k}}^2|\mathbf{h}_{n\mathbf{k}}\rangle. \tag{36}$$

The gradient of the ket vector can be expressed as

$$\nabla_{\mathbf{k}}|\mathbf{h}_{n\mathbf{k}}\rangle = \sum_{\mathbf{b}} w_{\mathbf{b}}\mathbf{b}(|\mathbf{h}_{n\mathbf{k}+\mathbf{b}}\rangle - |\mathbf{h}_{n\mathbf{k}}\rangle) \tag{37}$$

and its norm squared is given by

$$\|\nabla_{\mathbf{k}}\mathbf{h}_{n\mathbf{k}}\|^2 = \sum_{\mathbf{b}} w_{\mathbf{b}}\|\mathbf{h}_{n\mathbf{k}+\mathbf{b}} - \mathbf{h}_{n\mathbf{k}}\|^2. \tag{38}$$

Here, $\|\mathbf{A}\|^2=\langle \mathbf{A}|\mathbf{A}\rangle$ and $\mathbf{b}$ is a vector connecting each $\mathbf{k}$ point to its nearest neighbors in a simple cubic discretization mesh of the $\mathbf{k}$ space. $w_{\mathbf{b}}$ is the associated weight and satisfies $\Sigma_{\mathbf{b}} w_{\mathbf{b}} b_\alpha b_\beta = \delta_{\alpha\beta}$, where b_α is the x, y, or z component of $\mathbf{b}$. Then,

$$\bar{\mathbf{r}}_n = i\frac{v}{(2\pi)^d}\int_{\mathrm{BZ}} d\mathbf{k}\langle \mathbf{h}_{n\mathbf{k}}|\nabla_{\mathbf{k}}|\mathbf{h}_{n\mathbf{k}}\rangle = \frac{i}{N_{kp}}\sum_{\mathbf{k},\mathbf{b}} w_{\mathbf{b}}\mathbf{b}(\langle \mathbf{h}_{n\mathbf{k}}|\mathbf{h}_{n\mathbf{k}+\mathbf{b}}\rangle - 1) \tag{39}$$

and

$$\langle r^2\rangle_n = \frac{v}{(2\pi)^d}\int_{\mathrm{BZ}} d\mathbf{k}\|\nabla_{\mathbf{k}}\mathbf{h}_{n\mathbf{k}}\|^2 = \frac{2}{N_{kp}}\sum_{\mathbf{k},\mathbf{b}} w_{\mathbf{b}}(1-\mathrm{Re}\langle \mathbf{h}_{n\mathbf{k}}|\mathbf{h}_{n\mathbf{k}+\mathbf{b}}\rangle), \tag{40}$$

where N_{kp} is the number of discrete $\mathbf{k}$ points in the first BZ, and Re means the real part. Ω is represented as a $\mathbf{k}$ summation by a set of overlap matrices,

$$M_{mn}^{(\mathbf{k},\mathbf{b})} = \langle \mathbf{h}_{m\mathbf{k}}|\mathbf{h}_{n\mathbf{k}+\mathbf{b}}\rangle. \tag{41}$$

By iterative calculations based on the steepest descent method, we obtain the set of unitary transformations $U_{mn}^{(\mathbf{k})}$ that minimizes the spread functional. Details of the minimization of Ω are provided in Appendix B.

Rapid convergence to the maximally localized orbitals, defined by minimization of Ω, depends crucially on the initial guess of the MLWF's. In electronic systems, an initial guess for the shapes of the MLWF's follows from the atomic orbitals, s, p, and d, etc. In PC's, however, such a natural basis set does not exist. Therefore, we consider an alternative starting point. The $\mathbf{k}=0$ (Γ-point) distributions $\mathbf{H}_{n0}^{(0)}(\mathbf{r})=\mathbf{h}_{\mathbf{n0}}^{(0)}(\mathbf{r})$ exhibit fundamental symmetries related to the point group of the PC. This suggests that initial guess for the shapes of the WF's can be chosen from the Γ-point distributions. The Γ-point distributions can be chosen real, since the operator $\nabla\times\epsilon_p^{-1}(\mathbf{r})\nabla\times$ in Eq. (1) is Hermitian. Accordingly, we define initial trial WF's $\mathbf{g}_n(\mathbf{r})$ as

$$\mathbf{g}_n(\mathbf{r}) = \mathbf{h}_{\mathbf{n0}}^{(0)}(\mathbf{r})\exp[-(\mathbf{r}-\mathbf{r}^{(n)})^2/\sigma^2]. \tag{42}$$

Here $\mathbf{r}^{(n)}$ is the center point of $\mathbf{g}_n(\mathbf{r})$ and σ is the spatial extent of a Gaussian function. σ is a variational parameter. In comparison to exponential decay functions, the Gaussian function provided the most rapid convergence to the final MLWF's. We describe the choice of $\mathbf{r}^{(n)}$ and σ for specific PC's in Sec. IV. We project $\mathbf{g}_n(\mathbf{r})$ onto N Bloch functions at each $\mathbf{k}$ point.

$$|\tilde{\mathbf{H}}_{n\mathbf{k}}\rangle = \sum_{m=1}^{N}|\mathbf{H}_{m\mathbf{k}}^{(0)}\rangle\langle \mathbf{H}_{m\mathbf{k}}^{(0)}|\mathbf{g}_n\rangle = \sum_{m=1}^{N} A_{mn}|\mathbf{H}_{m\mathbf{k}}^{(0)}\rangle, \tag{43}$$

where $A_{mn}=\langle \mathbf{H}_{m\mathbf{k}}^{(0)}|\mathbf{g}_n\rangle$. Since these are not orthonormal, we modify them as follows:

$$|\mathbf{H}_{n\mathbf{k}}^{(l)}\rangle = \sum_{m=1}^{N} S_{mn}^{-1/2}|\tilde{\mathbf{H}}_{m\mathbf{k}}\rangle = \sum_{m=1}^{N}(AS^{-1/2})_{mn}|\mathbf{H}_{m\mathbf{k}}^{(0)}\rangle, \tag{44}$$

where $S_{mn}=\langle \tilde{\mathbf{H}}_{m\mathbf{k}}|\tilde{\mathbf{H}}_{n\mathbf{k}}\rangle=(A^\dagger A)_{mn}$ and $AS^{-1/2}$ is the unitary matrix. These initial Bloch functions satisfy the orthogonality relation, and the iterative minimization of Ω starts from them. From the definition (41), it is clear that $M_{nn}^{(\mathbf{k},\mathbf{b})}$ is close to unity for sufficiently small discretization mesh in $\mathbf{k}$ space. However, for a poor initial guess (42), $M_{nn}^{(\mathbf{k},\mathbf{b})}$ becomes much smaller than 1 or negative, leading to the divergence of the iterative calculations. Therefore, we must make a judicious choice of $\mathbf{r}^{(n)}$ and σ in Eq. (42) to ensure that $M_{nn}^{(\mathbf{k},\mathbf{b})}\sim 1$. In order to obtain Wannier functions that exhibit symmetries of the PC, we choose high symmetric points $\mathbf{r}^{(n)}$ in the PC. For example, in 2D square-lattice PC's, $(0,\ 0)$, $(\pm 0.5a, 0)$, $(0, \pm 0.5a)$, and $(\pm 0.5a, \pm 0.5a)$ are chosen as possible center points of the WF's. While the set of required $\mathbf{r}^{(n)}$ is not unique, we choose a combination of $\mathbf{r}^{(n)}$ such that $M_{nn}^{(\mathbf{k},\mathbf{b})}\sim 1$. The resulting MLWF's exhibit symmetries related to the point group of the underlying PC.

When constructing WF's, we consider a spectral range covering at least N complete photonic bands (outer frequency window). Within the outer frequency window, we

define $N_{\mathbf{k}}$ as the number of the photonic bands at each $\mathbf{k}$ point. When $N_{\mathbf{k}}=N$ at all $\mathbf{k}$ points, we can directly use the above MLWF method. When photonic bands overlap in frequency, it is possible for $N_{\mathbf{k}}>N$ over some ranges of $\mathbf{k}$ points. In this case, we must construct N equivalent photonic bands (pseudophotonic bands) from these $N_{\mathbf{k}}$ crossing photonic bands. When $N_{\mathbf{k}}=N$ at all $\mathbf{k}$ points, Ω_I is invariant. When $N_{\mathbf{k}}>N$, however, we must minimize Ω_I before considering the minimization of Ω. Although pseudophotonic bands may be slightly different from original photonic bands, our construction aims to preserve the properties of the PBG. In this way, we can accurately describe defect modes. In practice, the pseudophotonic bands coincide with the original photonic bands within a reduced spectral range (inner frequency window). Details of constructing pseudophotonic bands are provided in Appendix B.

III. WANNIER FUNCTIONS IN MICROCHIP LAYERS

A. 3D structures with 2D periodicity

In this section, we describe the general method of constructing WF's in 2D-3D PBG heterostructures[5,6,24,25] and 2D membrane PC's.[4] This begins with evaluation of the photonic band structure, based on the supercell technique. 2D microchip layers in 2D-3D PBG heterostructures (see Figs. 12 and 17) and 2D membrane PC's are assumed to be parallel to the 2D xy plane. Since periodic boundary conditions are imposed in the z direction through the supercell, we must modify the WF method from that of bulk 3D PBG crystals. A magnetic field $\mathbf{H}(\mathbf{r}_\parallel,z)$ satisfies the equation,

$$\nabla\times\{\epsilon_p^{-1}(\mathbf{r}_\parallel,z)\,\nabla\times\mathbf{H}(\mathbf{r}_\parallel,z)\}=\frac{\omega^2}{c^2}\mathbf{H}(\mathbf{r}_\parallel,z), \tag{45}$$

where $\parallel$ indicates the 2D coordinate spanning the xy plane, and $\epsilon_p(\mathbf{r}_\parallel,z)$ is the dielectric index of the periodic heterostructure. We impose periodic boundary conditions in the z direction of the form $\epsilon_p(\mathbf{r}_\parallel,z)=\epsilon_p(\mathbf{r}_\parallel+\mathbf{R}_\parallel,z+L)$, where $\mathbf{R}_\parallel$ is an arbitary lattice vector in the 2D plane, and L is the vertical length of the supercell. A Bloch function of the magnetic field is expressed as

$$\mathbf{H}^{(0)}_{n\mathbf{k}_\parallel}(\mathbf{r}_\parallel,z)=e^{i\mathbf{k}_\parallel\cdot\mathbf{r}_\parallel}\mathbf{h}^{(0)}_{n\mathbf{k}_\parallel}(\mathbf{r}_\parallel,z), \tag{46}$$

where the periodic part of the Bloch function is defined as follows:

$$\mathbf{h}^{(0)}_{n\mathbf{k}_\parallel}(\mathbf{r}_\parallel,z)=\sum_{\mathbf{G}_\parallel}\sum_{G_z}\mathbf{h}^{(0)}_{n\mathbf{k}_\parallel}(\mathbf{G}_\parallel,G_z)e^{i(\mathbf{G}_\parallel\cdot\mathbf{r}_\parallel+G_z z)}. \tag{47}$$

Here, $\mathbf{G}_\parallel$ and G_z are the reciprocal lattice vectors in the 2D plane and z direction, respectively. n and $\mathbf{k}_\parallel$ indicate the photonic band number and the 2D wave vector, respectively. The Bloch functions satisfy an orthogonality:

$$\langle\mathbf{H}^{(0)}_{n\mathbf{k}_\parallel}|\mathbf{H}^{(0)}_{n'\mathbf{k}'_\parallel}\rangle=\frac{(2\pi)^2}{v_{2\mathrm{D}}}\delta_{nn'}\delta(\mathbf{k}_\parallel-\mathbf{k}'_\parallel), \tag{48}$$

where we define the matrix element

$$\langle\mathbf{A}|f|\mathbf{B}\rangle=\int_{V_{2\mathrm{D}}}d^2\mathbf{r}_\parallel\int_{-L/2}^{L/2}dz f(\mathbf{r}_\parallel,z)\mathbf{A}^*(\mathbf{r}_\parallel,z)\cdot\mathbf{B}(\mathbf{r}_\parallel,z). \tag{49}$$

Here f is a general scalar function, $\mathbf{A}$ and $\mathbf{B}$ are general vector functions, integration is over the entire 2D volume $V_{2\mathrm{D}}$, and $v_{2\mathrm{D}}$ is the volume of the 2D unit cell in the 2D xy plane. Defining $\mathbf{H}_{n\mathbf{k}_\parallel}(\mathbf{r}_\parallel,z)=\Sigma_{m=1}^{N}U^{(\mathbf{k}_\parallel)}_{mn}\mathbf{H}^{(0)}_{m\mathbf{k}_\parallel}(\mathbf{r}_\parallel,z)$, the WF of the magnetic field $\mathbf{W}^{(\mathbf{H})}_{n\mathbf{R}_\parallel}(\mathbf{r}_\parallel,z)$ $(n=1,2,\ldots,N)$, centered at position $\mathbf{R}_\parallel$, is then given by

$$\mathbf{W}^{(\mathbf{H})}_{n\mathbf{R}_\parallel}(\mathbf{r}_\parallel,z)=\frac{v_{2\mathrm{D}}}{(2\pi)^2}\int_{\mathrm{BZ}}d^2\mathbf{k}_\parallel e^{-i\mathbf{k}_\parallel\cdot\mathbf{R}_\parallel}\mathbf{H}_{n\mathbf{k}_\parallel}(\mathbf{r}_\parallel,z), \tag{50}$$

$$\mathbf{H}_{n\mathbf{k}_\parallel}(\mathbf{r}_\parallel,z)=\sum_{\mathbf{R}_\parallel}e^{i\mathbf{k}_\parallel\cdot\mathbf{R}_\parallel}\mathbf{W}^{(\mathbf{H})}_{n\mathbf{R}_\parallel}(\mathbf{r}_\parallel,z), \tag{51}$$

where the latter sum is over the set of all direct lattice vectors $\mathbf{R}_\parallel$.

Unlike bulk 3D WF's, integration of the Bloch function is over only 2D $\mathbf{k}_\parallel$ spaces. Therefore, $\mathbf{W}^{(\mathbf{H})}_{n\mathbf{R}_\parallel}(\mathbf{r}_\parallel,z)$ is localized only in the 2D xy plane. We impose a periodicity in the z direction, $\mathbf{W}^{(\mathbf{H})}_{n\mathbf{R}_\parallel}(\mathbf{r}_\parallel,z)=\mathbf{W}^{(\mathbf{H})}_{n\mathbf{R}_\parallel}(\mathbf{r}_\parallel,z+L)$. This construction is widely used in supercell techniques that model a PC membrane[4] or a microchip layer in a 2D-3D PBG heterostructure. When the vertical periodicity scale is made sufficiently large (typically $L\geqslant 3a$, where a is the lattice constant), the optical properties of the single 2D layer can be extracted from periodic array of supercells. In particular, optical modes that are exponentially confined to a single 2D layer become insensitive to L for sufficiently large L. $\mathbf{W}^{(\mathbf{H})}_{n\mathbf{R}_\parallel}(\mathbf{r}_\parallel,z)$ satisfies the orthogonality relation

$$\langle\mathbf{W}^{(\mathbf{H})}_{n\mathbf{R}_\parallel}|\mathbf{W}^{(\mathbf{H})}_{n'\mathbf{R}'_\parallel}\rangle=\delta_{nn'}\delta_{\mathbf{R}_\parallel\mathbf{R}'_\parallel}. \tag{52}$$

Here we use the definition (49) with $f=1$. Since the operator $\nabla\times\epsilon_p^{-1}(\mathbf{r}_\parallel,z)\nabla\times$ in Eq. (45) is Hermitian, we can impose the symmetries $\mathbf{H}_{n\mathbf{k}_\parallel}(\mathbf{r}_\parallel,z)=\mathbf{H}^*_{n-\mathbf{k}_\parallel}(\mathbf{r}_\parallel,z)$ and $U^{(\mathbf{k}_\parallel)}_{mn}=U^{(-\mathbf{k}_\parallel)^*}_{mn}$. In this case, the WF's of the magnetic fields can be chosen real. We now consider an expansion of the magnetic field in Eq. (45) in the basis of WF's defined by Eq. (51),

$$\mathbf{H}(\mathbf{r}_\parallel,z)=\sum_{n=1}^{N}\sum_{\mathbf{R}_\parallel}c_n e^{i\mathbf{k}_\parallel\cdot\mathbf{R}_\parallel}\mathbf{W}^{(\mathbf{H})}_{n\mathbf{R}_\parallel}(\mathbf{r}_\parallel,z), \tag{53}$$

where c_n are undetermined coefficients.

By substituting Eq. (53) into Eq. (45) and using the orthogonality of the WF's, the following eigenvalue equation is obtained:

$$\sum_{n'=1}^{N}\left(\sum_{\mathbf{R}'_\parallel}e^{i\mathbf{k}_\parallel\cdot\mathbf{R}'_\parallel}A^{nn'}_{\mathbf{0}_\parallel\mathbf{R}'_\parallel}\right)c_{n'}=\frac{\omega^2}{c^2}c_n, \tag{54}$$

where the tight-binding matrix element is defined as

$$A^{nn'}_{\mathbf{R}_\parallel\mathbf{R}'_\parallel} \equiv \langle \mathbf{W}^{(\mathbf{H})}_{n\mathbf{R}_\parallel} | \nabla \times \epsilon_p^{-1} \nabla \times | \mathbf{W}^{(\mathbf{H})}_{n'\mathbf{R}'_\parallel} \rangle = \frac{v_{2\mathrm{D}}}{(2\pi)^2} \int_{\mathrm{BZ}} d^2\mathbf{k}_\parallel e^{i\mathbf{k}_\parallel\cdot(\mathbf{R}_\parallel-\mathbf{R}'_\parallel)} \sum_{m=1}^{N} U^{(\mathbf{k}_\parallel)\dagger}_{nm} \left(\frac{\omega_{m\mathbf{k}_\parallel}}{c}\right)^2 U^{(\mathbf{k}_\parallel)}_{mn'}. \tag{55}$$

By solving the eigenvalue matrix in Eq. (54), the photonic band structure is reproduced by the WF basis. When the WF's are very well localized, $A^{nn'}_{\mathbf{R}_\parallel\mathbf{R}'_\parallel}$ decays rapidly with increasing $|\mathbf{R}_\parallel-\mathbf{R}'_\parallel|$, and we can take a small number of the lattice vectors $\mathbf{R}_\parallel$ in Eq. (54). In the case of MLWF's we can typically ignore matrix elements for which $|\mathbf{R}_\parallel-\mathbf{R}'_\parallel|>4a$.

The WF's of magnetic fields can be expressed in terms of electric fields using the Maxwell equation. The electric field Bloch function $\mathbf{E}^{(0)}_{n\mathbf{k}_\parallel}(\mathbf{r}_\parallel,z)$ satisfies the orthogonality relation,

$$\langle \mathbf{E}^{(0)}_{n\mathbf{k}_\parallel} | \epsilon_p | \mathbf{E}^{(0)}_{n'\mathbf{k}'_\parallel} \rangle = \frac{(2\pi)^2}{v_{2\mathrm{D}}} \delta_{nn'}\delta(\mathbf{k}_\parallel-\mathbf{k}'_\parallel). \tag{56}$$

Defining $\mathbf{E}_{n\mathbf{k}_\parallel}(\mathbf{r}_\parallel,z)=\Sigma_{m=1}^{N} U^{(\mathbf{k}_\parallel)}_{mn}\mathbf{E}^{(0)}_{m\mathbf{k}_\parallel}(\mathbf{r}_\parallel,z)$, the WF's of the electric fields $\mathbf{W}^{(\mathbf{E})}_{n\mathbf{R}_\parallel}(\mathbf{r}_\parallel,z)$ are given by

$$\mathbf{W}^{(\mathbf{E})}_{n\mathbf{R}_\parallel}(\mathbf{r}_\parallel,z) = \frac{v_{2\mathrm{D}}}{(2\pi)^2} \int_{\mathrm{BZ}} d^2\mathbf{k}_\parallel e^{-i\mathbf{k}_\parallel\cdot\mathbf{R}_\parallel} \mathbf{E}_{n\mathbf{k}_\parallel}(\mathbf{r}_\parallel,z). \tag{57}$$

$\mathbf{W}^{(\mathbf{E})}_{n\mathbf{R}_\parallel}(\mathbf{r}_\parallel,z)$ is localized only in the 2D xy plane, and has a periodicity in the z direction, $\mathbf{W}^{(\mathbf{E})}_{n\mathbf{R}_\parallel}(\mathbf{r}_\parallel,z)=\mathbf{W}^{(\mathbf{E})}_{n\mathbf{R}_\parallel}(\mathbf{r}_\parallel,z+L)$. $\mathbf{W}^{(\mathbf{E})}_{n\mathbf{R}_\parallel}(\mathbf{r}_\parallel,z)$ satisfies the orthogonality relation

$$\langle \mathbf{W}^{(\mathbf{E})}_{n\mathbf{R}_\parallel} | \epsilon_p | \mathbf{W}^{(\mathbf{E})}_{n'\mathbf{R}'_\parallel} \rangle = \delta_{nn'}\delta_{\mathbf{R}_\parallel\mathbf{R}'_\parallel}. \tag{58}$$

Since $\mathbf{H}_{n\mathbf{k}_\parallel}(\mathbf{r}_\parallel,z)=\mathbf{H}^*_{n-\mathbf{k}_\parallel}(\mathbf{r}_\parallel,z)$ and $U^{(\mathbf{k}_\parallel)}_{mn}=U^{(-\mathbf{k}_\parallel)*}_{mn}$, it follows that $\mathbf{E}_{n\mathbf{k}_\parallel}(\mathbf{r}_\parallel,z)=-\mathbf{E}^*_{n-\mathbf{k}_\parallel}(\mathbf{r}_\parallel,z)$. Therefore, the WF's of the electric fields are pure imaginary.

B. Defects and surface polarization charge

In the presence of a dielectric defect $\delta\epsilon(\mathbf{r}_\parallel,z)$ in 2D-3D PBG heterostructure and 2D membrane PC's, we start with the electric-field Maxwell wave equation.

$$\nabla\times\{\nabla\times\mathbf{E}(\mathbf{r}_\parallel,z)\} = \frac{\omega^2}{c^2}\epsilon(\mathbf{r}_\parallel,z)\mathbf{E}(\mathbf{r}_\parallel,z), \tag{59}$$

$$\nabla\cdot\{\epsilon(\mathbf{r}_\parallel,z)\mathbf{E}(\mathbf{r}_\parallel,z)\} = 0, \tag{60}$$

where $\epsilon(\mathbf{r}_\parallel,z)=\epsilon_p(\mathbf{r}_\parallel,z)+\delta\epsilon(\mathbf{r}_\parallel,z)$. We expand the electric field in the basis of the MLWF's referring to Eq. (17),

$$\mathbf{E}(\mathbf{r}_\parallel,z) = \sum_{n\mathbf{R}_\parallel} E_{n\mathbf{R}_\parallel} \tilde{\mathbf{W}}^{(\mathbf{E})}_{n\mathbf{R}_\parallel}(\mathbf{r}_\parallel,z), \tag{61}$$

where $E_{n\mathbf{R}_\parallel}$ is the expansion coefficient and $\tilde{\mathbf{W}}^{(\mathbf{E})}_{n\mathbf{R}_\parallel}(\mathbf{r}_\parallel,z) = \mathbf{W}^{(\mathbf{E})}_{n\mathbf{R}_\parallel}(\mathbf{r}_\parallel,z)-\nabla\phi_{n\mathbf{R}_\parallel}(\mathbf{r}_\parallel,z)$. Here $\phi_{n\mathbf{R}_\parallel}(\mathbf{r}_\parallel,z)$ is a scalar potential satisfying the Poisson equation,

$$\nabla\cdot\{\epsilon(\mathbf{r}_\parallel,z)\nabla\phi_{n\mathbf{R}_\parallel}(\mathbf{r}_\parallel,z)\} = \nabla\cdot\{\delta\epsilon(\mathbf{r}_\parallel,z)\mathbf{W}^{(\mathbf{E})}_{n\mathbf{R}_\parallel}(\mathbf{r}_\parallel,z)\}. \tag{62}$$

Details of solving the Poisson equation are discussed in Appendix A. By substituting Eq. (61) into Eq. (59) and using the orthogonality of the WF's, a matrix equation can be obtained,

$$\sum_{n'\mathbf{R}'_\parallel} A^{nn'}_{\mathbf{R}_\parallel\mathbf{R}'_\parallel} E_{n'\mathbf{R}'_\parallel} = \frac{\omega^2}{c^2} \sum_{n'\mathbf{R}'_\parallel} \{\delta_{nn'}\delta_{\mathbf{R}_\parallel\mathbf{R}'_\parallel} + D^{nn'}_{\mathbf{R}_\parallel\mathbf{R}'_\parallel} + F^{nn'}_{\mathbf{R}_\parallel\mathbf{R}'_\parallel}\} E_{n'\mathbf{R}'_\parallel}, \tag{63}$$

where

$$A^{nn'}_{\mathbf{R}_\parallel\mathbf{R}'_\parallel} \equiv \langle \mathbf{W}^{(\mathbf{E})}_{n\mathbf{R}_\parallel} | \nabla \times \nabla \times | \mathbf{W}^{(\mathbf{E})}_{n'\mathbf{R}'_\parallel} \rangle = \frac{v_{2\mathrm{D}}}{(2\pi)^2} \int_{\mathrm{BZ}} d^2\mathbf{k}_\parallel e^{i\mathbf{k}_\parallel\cdot(\mathbf{R}_\parallel-\mathbf{R}'_\parallel)} \sum_{m=1}^{N} U^{(\mathbf{k}_\parallel)\dagger}_{nm} \left(\frac{\omega_{m\mathbf{k}_\parallel}}{c}\right)^2 U^{(\mathbf{k}_\parallel)}_{mn'}, \tag{64}$$

$$D^{nn'}_{\mathbf{R}_\parallel\mathbf{R}'_\parallel} \equiv \langle \mathbf{W}^{(\mathbf{E})}_{n\mathbf{R}_\parallel} | \delta\epsilon | \mathbf{W}^{(\mathbf{E})}_{n'\mathbf{R}'_\parallel} \rangle \tag{65}$$

and

$$F^{nn'}_{\mathbf{R}_\parallel\mathbf{R}'_\parallel} \equiv -\langle \mathbf{W}^{(\mathbf{E})}_{n\mathbf{R}_\parallel} | \epsilon_p + \delta\epsilon | \nabla\phi_{n'\mathbf{R}'_\parallel} \rangle = -\langle \mathbf{W}^{(\mathbf{E})}_{n\mathbf{R}_\parallel} | \delta\epsilon | \nabla\phi_{n'\mathbf{R}'_\parallel} \rangle. \tag{66}$$

$A^{nn'}_{\mathbf{R}_\parallel\mathbf{R}'_\parallel}$ is the tight-binding matrix element, and $D^{nn'}_{\mathbf{R}_\parallel\mathbf{R}'_\parallel}$ and $F^{nn'}_{\mathbf{R}_\parallel\mathbf{R}'_\parallel}$ are the overlap matrix elements of the WF's with the defect structures. In Eq. (66), we used $\langle \mathbf{W}^{(\mathbf{E})}_{n\mathbf{R}_\parallel} | \epsilon_p | \nabla\phi_{n'\mathbf{R}'_\parallel} \rangle = -\langle \nabla\cdot(\epsilon_p \mathbf{W}^{(\mathbf{E})}_{n\mathbf{R}_\parallel}) | \phi_{n'\mathbf{R}'_\parallel} \rangle = 0$. When these matrix elements decay rapidly with increasing $|\mathbf{R}_\parallel-\mathbf{R}'_\parallel|$, the matrix equation becomes sparse. $A^{nn'}_{\mathbf{R}_\parallel\mathbf{R}'_\parallel}$, $D^{nn'}_{\mathbf{R}_\parallel\mathbf{R}'_\parallel}$, and $F^{nn'}_{\mathbf{R}_\parallel\mathbf{R}'_\parallel}$ are Hermitian.

C. Maximally localized optical orbitals

In 2D-3D PBG heterostructures and 2D membrane PC's, maximally localized orbitals are defined by the unitary transformation that minimizes the transverse spread functional:

$$\Omega = \sum_{n=1}^{N} (\langle r_\parallel^2\rangle_n - (\bar{\mathbf{r}}_{\parallel n})^2), \tag{67}$$

where

$$\bar{\mathbf{r}}_{\parallel n} = \langle \mathbf{W}^{(\mathbf{H})}_{n\mathbf{0}_\parallel} | \mathbf{r}_\parallel | \mathbf{W}^{(\mathbf{H})}_{n\mathbf{0}_\parallel} \rangle \tag{68}$$

and

$$\langle r_\parallel^2\rangle_n = \langle \mathbf{W}^{(\mathbf{H})}_{n\mathbf{0}_\parallel} | \mathbf{r}_\parallel^2 | \mathbf{W}^{(\mathbf{H})}_{n\mathbf{0}_\parallel} \rangle. \tag{69}$$

Ω can be represented by a set of overlap matrices,

$$M^{(\mathbf{k}_\parallel,\mathbf{b}_\parallel)}_{mn} = \langle \mathbf{h}_{m\mathbf{k}_\parallel} | \mathbf{h}_{n\mathbf{k}_\parallel+\mathbf{b}_\parallel} \rangle, \tag{70}$$

where $\mathbf{b}_\parallel$ is a vector connecting each $\mathbf{k}_\parallel$ point to its nearest neighbors in a discretization mesh, and $U^{(\mathbf{k}_\parallel)}_{mn}$ is implicit

through the definition $|\mathbf{h}_{n\mathbf{k}_\parallel}\rangle = \Sigma_{m=1}^{N} U_{mn}^{(\mathbf{k}_\parallel)} |\mathbf{h}_{m\mathbf{k}_\parallel}^{(0)}\rangle$. The procedure of minimizing the spread functional is the same as that in bulk PBG crystals.

Initial trial WF's $\mathbf{g}_n(\mathbf{r}_\parallel, z)$ are defined as follows:

$$\mathbf{g}_n(\mathbf{r}_\parallel, z) = \mathbf{h}_{n\mathbf{0}_\parallel}^{(0)}(\mathbf{r}_\parallel, z)\exp[-(\mathbf{r}_\parallel - \mathbf{r}_\parallel^{(n)})^2/\sigma^2], \tag{71}$$

where $\mathbf{r}_\parallel^{(n)}$ is the center point of $\mathbf{g}_n(\mathbf{r}_\parallel, z)$, and σ is the spatial extent of a Gaussian function. We describe $\mathbf{r}_\parallel^{(n)}$ and σ for specific PC in Sec. IV. $\mathbf{h}_{n0_\parallel}^{(0)}(\mathbf{r}_\parallel, z)$ is the Γ-point distribution. This function is localized only in the 2D xy plane, and has a periodicity in the z direction, $\mathbf{g}_n(\mathbf{r}_\parallel, z) = \mathbf{g}_n(\mathbf{r}_\parallel, z+L)$. By projecting $\mathbf{g}_n(\mathbf{r}_\parallel, z)$ onto N Bloch functions at each $\mathbf{k}_\parallel$ point and orthonormalizing, initial Bloch functions $|\mathbf{H}_{n\mathbf{k}_\parallel}^{(I)}\rangle$ can be obtained,

$$|\mathbf{H}_{n\mathbf{k}_\parallel}^{(I)}\rangle = \sum_{m=1}^{N} (AS^{-1/2})_{mn} |\mathbf{H}_{m\mathbf{k}_\parallel}^{(0)}\rangle, \tag{72}$$

where $A_{mn} = \langle \mathbf{H}_{m\mathbf{k}_\parallel}^{(0)} | \mathbf{g}_n \rangle$, $S_{mn} = (A^\dagger A)_{mn}$, and $AS^{-1/2}$ is the unitary matrix. Iterative calculations of minimizing Ω start from these initial conditions.

IV. NUMERICAL RESULTS USING LOCALIZED LIGHT ORBITALS

We begin by reviewing and extending the optical WF method to idealized 2D photonic crystals. The TM modes, in which the electric field vector is normal to the plane of periodicity, have already been studied by others.[12] In this case, there is no requirement for modification of the WF's in the presence of defects. Here there is no surface polarization charge and the problem reduces to that of a scalar wave function which remains continuous across dielectric interfaces. A nontrivial generalization of the 2D WF arises in the case of TE modes, in which the electric field lies in the plane of periodicity. In this case defects introduce modifications of the optical orbitals and surface polarization charges must be carefully taken into account. After demonstrating the use of localized light orbitals in these idealized 2D architectures, we proceed to present numerical results and comparisons for a variety of 3D PBG structures.

A. TM mode in 2D PBG structures

In a TM mode, we consider the square-lattice PC composed of GaAs circular dielectric rods. The dielectric index of GaAs is $\epsilon = 11.56$, and a background is the air. The radius of rods is $R/a = 0.18$, where a is the lattice constant. In Fig. 1, we show the photonic band structure. Solid lines indicate the photonic band structure calculated with 441 plane waves by the PWE method, and this structure has a 2D PBG of 37.9% (gap to midgap ratio). In this mode, electric and magnetic fields are parallel to the z direction and the 2D xy plane, respectively. Therefore, we focus only on the scalar electric field. Unlike the method described in Sec. II, we construct four MLWF's of electric fields directly from the first four photonic bands, according to previous work.[12] We take 40 $\times$40 $\mathbf{k}$ points in the whole first BZ when constructing the

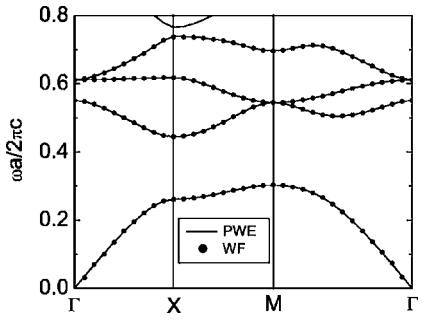

FIG. 1. Photonic band structure for the 2D TM mode of a square-lattice PC composed of GaAs circular dielectric rods. The dielectric index of GaAs is $\epsilon = 11.56$ and the background is air. The radius of rods is $R/a = 0.18$, where a is the lattice constant. Solid lines indicate the photonic band structure calculated by the PWE method, and black points indicate that reproduced by the MLWF's.

MLWF's. Black points indicate the photonic band structure reproduced by the MLWF's. When reproducing the photonic band structure with the tight-binding wave equation, we consider overlap matrix elements of optical WF's separated by as far as four lattice constants. As shown in Fig. 1, the solid lines (PWE) and the black points (MLWF method) coincide.

In Fig. 2, we show four MLWF's of E_z. When in each figure a center rod is arranged at (0,0), we set up the center point of the second initial trial WF at $(0.5a, 0.5a)$ and those of the first, third, and fourth initial trial WF's at (0,0). In an electric-field version of Eq. (42), we take $\sigma = 0.3a$. In comparison to wider spatial extents such as $\sigma = 1.0a$, $\sigma = 0.3a$ provides fast convergence of the final MLWF's. Although the first, third, and fourth MLWF's are localized at dielectric rods, the second MLWF is localized in air regions. The dis-

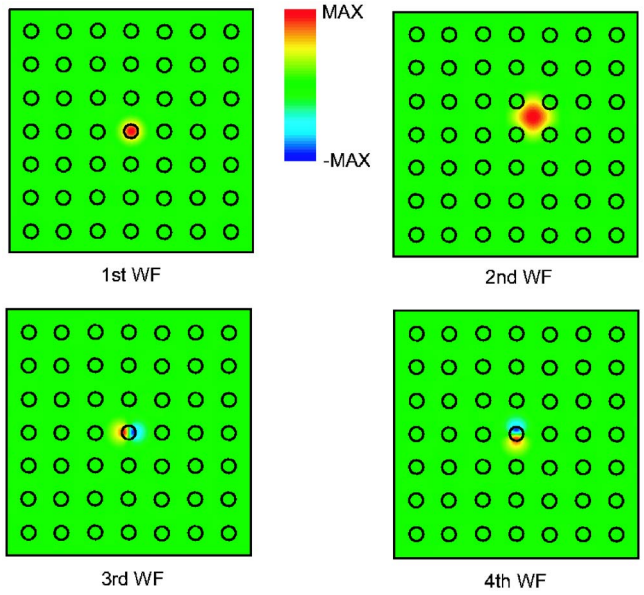

FIG. 2. (Color online) The 1st–4th MLWF's of E_z in the square-lattice PC in the 2D TM mode. Although the first, third, and fourth MLWF's are localized at dielectric rods, the second MLWF is localized in air regions. The distributions of the third and fourth MLWF's are identical except for a 90° rotation.

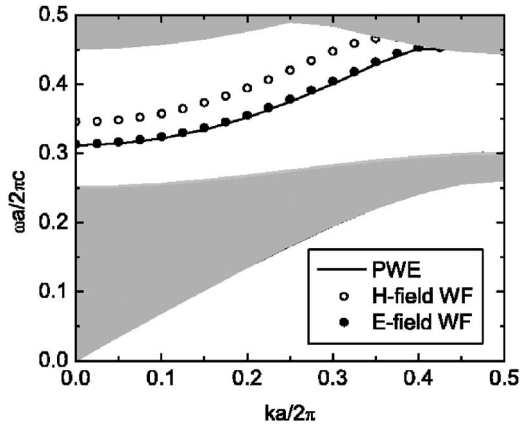

FIG. 3. Single guided mode in the case of removing one line of rods in the square-lattice PC in the 2D TM mode. A solid line indicates the single guided mode calculated by the PWE method, and white and black points indicate that calculated by the *H*-field and *E*-field optical WF methods, respectively. Shaded regions indicate the projected 2D photonic band structure.

tributions of the third and fourth MLWF's are identical except for a 90° rotation.

We consider a waveguide consisting of one removed line of rods. We apply the electric and magnetic-field optical WF methods in Eqs. (19) and (27) to the calculation of the guided mode. In the TM mode, the right-hand side in Eq. (18) is always zero because the electric field is always perpendicular to the 2D plane. Therefore, there is no electric field discontinuity due to surface polarization charges and we use the unmodified optical WF method. We consider overlap matrix elements of WF's separated by up to three lattice constants in the calculation of the guided mode in the tight-binding picture. Figure 3 shows the single guided mode in the optical WF method. In the air waveguide, it is possible to obtain the single guided mode in wide frequency regions. A solid line indicates the single guided mode calculated by the PWE method. Shaded regions indicate the projected 2D photonic band structure. White and black points indicate the single guided mode calculated by the magnetic and electric-field optical WF methods, respectively. As shown in Fig. 3, the solid line and the white points are very different. This discrepancy arises from the inability of the unmodified magnetic field WF to efficiently describe the boundary condition of the electromagnetic field at dielectric interfaces produced by defects. At dielectric interfaces, $\mathbf{n}(\mathbf{r})\times\{[\epsilon_p(\mathbf{r})+\delta\epsilon(\mathbf{r})]^{-1}\nabla\times\mathbf{H}(\mathbf{r})\}$, where $\mathbf{n}(\mathbf{r})$ is the normal vector to interfaces, should be continuous. This condition corresponds to the continuity of electric fields parallel to the interfaces. However, this condition is violated by unmodified magnetic WF's, since $\mathbf{n}(\mathbf{r})\times[\epsilon_p^{-1}(\mathbf{r})\nabla\times\mathbf{W}_{n\mathbf{R}}^{(\mathbf{H})}(\mathbf{r})]$ instead is continuous at defect interfaces. This means the magnetic-field optical WF method requires modification for defect modes even for the simplest case of TM modes. On the other hand, the unmodified electric field WF method offers high accuracy with a small number of localized light orbitals, in spite of a large perturbation, $\delta\epsilon(\mathbf{r})$, such as the removal of one line of the rods. In what follows we show that even the electric field orbitals require modification for 2D TE modes and in 3D architectures.

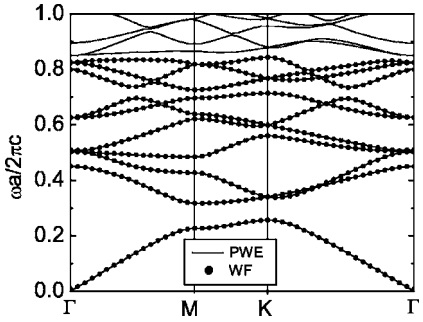

FIG. 4. Photonic band structure for the 2D TE mode of an idealized triangular-lattice PC composed of circular air holes in solid dielectric background. We choose the refractive index of the background to be $n=2.76$. The radius of air holes is $R/a=0.29$, where a is the lattice constant. This is an idealized version (limited to two spatial dimensions) of the physical 2D membrane PC with finite thickness in the third dimension described in Fig. 21. Solid lines indicate the photonic band structure calculated by the PWE method, and black points indicate that reproduced by the MLWF's.

B. TE mode in 2D PBG structures

In a TE mode, we consider the idealized triangular-lattice PC composed of circular air holes in solid dielectric background. We choose the refractive index of the background to be $n=2.76$. The radius of air holes is $R/a=0.29$, where a is the lattice constant. This is an idealized version (limited to two spatial dimensions) of the physical 2D membrane PC with finite thickness in the third dimension discussed below in Sec. IV E. This idealized structure is often used to provide a rough idea of the properties of realistic 2D membrane PC's. Considerably more computational effort is required to analyze the 2D membrane PC exactly, since it is a 3D architecture with translational symmetry in only two dimensions. We show in Sec. IV E how this can be analyzed using 3D WF's in a supercell.

In Fig. 4, we show the TE photonic band structure for the idealized 2D triangular lattice PC. Solid lines indicate the photonic band structure calculated with 441 plane waves by the PWE method. This structure has a 2D TE PBG of 21.0% (gap to midgap ratio). In the TE mode, electric and magnetic fields are parallel to the 2D xy plane and the z directions, respectively. The electric field vectors exhibit discontinuities across dielectric interfaces and for simplicity, we begin by considering the scalar magnetic field. We construct 10 MLWF's of magnetic fields from the first 10 photonic bands. We take 40×40 $\mathbf{k}$ points in the whole first BZ when constructing MLWF's. Black points indicate the photonic band structure reproduced by the MLWF's. When reproducing the photonic band structure, we consider up to the fourth neighbor (separated by up to four lattice constants) interactions. As shown in Fig. 4, the solid lines and the black points coincide.

In Fig. 5, we show the first, second, seventh, and eighth TE MLWF's of H_z. Color patterns are similar in some respects to those in Fig. 2 for the field E_z in the TM mode. When a specific hole center is designated as (0,0), we place the center point of the first initial trial WF at (0, 0) and those of the 2nd–10th initial trial WF's at $(a/2,\sqrt{3}a/6)$, which is the center of gravity of the triangle composed of three air

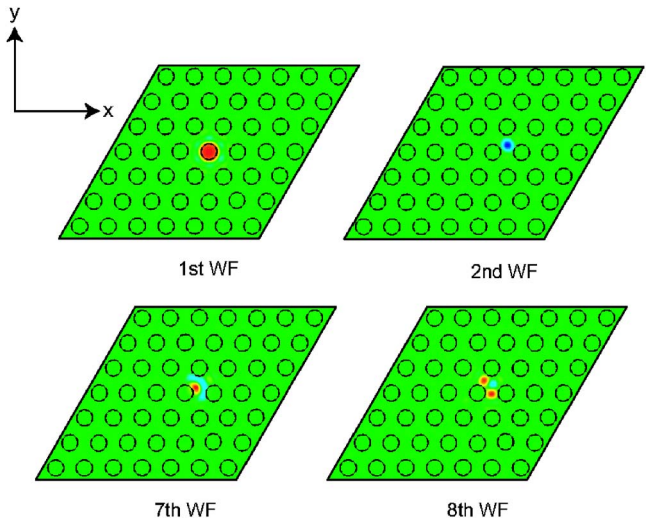

FIG. 5. (Color online) The first, second, seventh, and eighth MLWF's of H_z in the triangular-lattice PC in the 2D TE mode. Color patterns are the same as those in Fig. 2. In the 2D TE mode, MLWF's have more complicated shapes, than in the 2D TM mode.

holes. However, the center points of the MLWF's are generally different from those of the initial trial WF's. In Eq. (42), we take $\sigma=0.3a$. In the TE mode, MLWF's have more complicated shapes, than in the TM mode.

We first consider guided modes in the case of one missing line of air holes. Here, we convert our description to electric field localized light orbitals. When calculating the guided modes by the optical WF method in the TE mode, we must use the modified expansion representation of electric fields in Eq. (17). We consider up to the third neighbor (separated by up to three lattice constants) interactions in the construction of the tight-binding wave equation for guided modes by the optical WF representation. Figures 6(a) and 6(b) show the guided modes in the unmodified and modified optical WF methods, respectively. Since we can afford to take a large number of reciprocal lattice vectors in this idealized 2D system, the Gibbs phenomenon associated with dielectric interfaces is small (Appendix A). Therefore, results using the (smoothing) σ approximation are almost the same as without using it. We show only the case of using the σ approximation in the modified optical WF method. The inset indicates the structure of the dielectric waveguide. Solid lines indicate the guided modes calculated by the PWE method. Shaded regions indicate the projected 2D photonic band structure. Black points indicate the guided modes calculated by the optical WF method. In Fig. 6(a) the solid lines and the black points do not coincide at all. In Fig. 6(b) the black points are very close to the solid lines. Clearly, the key to applying the optical WF method in general architectures is the proper treatment of induced surface polarization charges.

As a second illustration, we consider an air waveguide, of width $2R$, in the triangular-lattice PC. Figure 7 shows the single guided mode in the optical WF method. A solid line indicates the guided mode calculated by the PWE method. White and black points indicate the guided modes calculated by the unmodified and modified optical WF methods, respectively. Once again, the accuracy of the localized light orbital

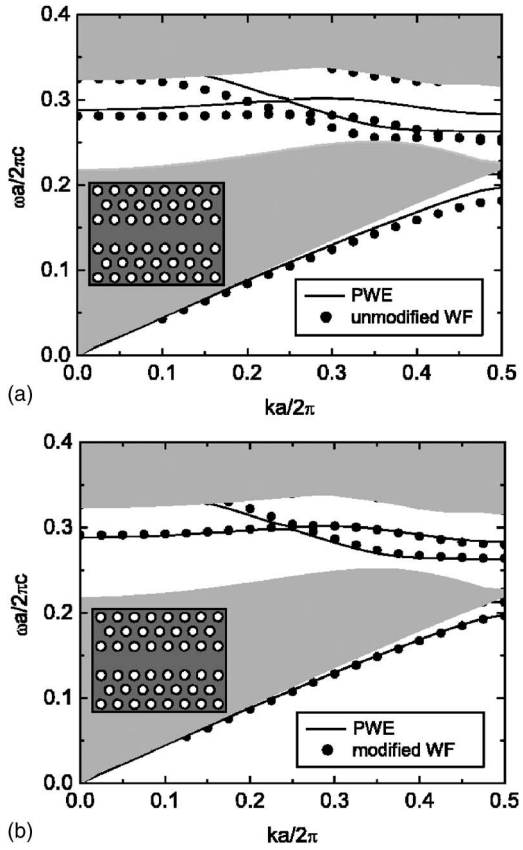

FIG. 6. Guided modes in the case of missing one line of air holes in the triangular-lattice PC in the 2D TE mode: (a) unmodified optical WF method and (b) modified optical WF method using the σ approximation. Solid lines indicate the guided modes calculated by the PWE method, and black points indicate those calculated by the optical WF method. Shaded regions indicate the projected 2D photonic band structure. The inset indicates the structure of the dielectric waveguide.

method hinges crucially on the proper treatment of induced polarization charge in defects. Clearly, the modified WF method is valid for a variety of different defect architectures.

C. 3D PBG structures

In three-dimensional periodic dielectric microstructures the full vector nature of the electromagnetic field must be incorporated into the WF's and induced polarization charges of defects must always be treated. Unlike idealized 2D systems, the dielectric structures within a given unit cell required to form a large 3D PBG are highly complex and lead to MLWF's with nontrivial and often unanticipated shapes. We consider first a 3D PBG Si woodpile structure.[32–34] The dielectric index of the Si woodpile is $\epsilon=11.9$ and the width and height of rods are chosen to be $d=0.25a$ and $h=0.3a$, respectively, where a is the distance between neighboring rods. Since one unit cell of the woodpile has four stacking layers, the periodicity of stacking layers is $c=4h=1.2a$. We consider the simple cubic structure $a\times a\times c$ as a unit cell. In Fig. 8, we show the photonic band structure. Solid lines indicate the photonic band structure calculated with 343 plane

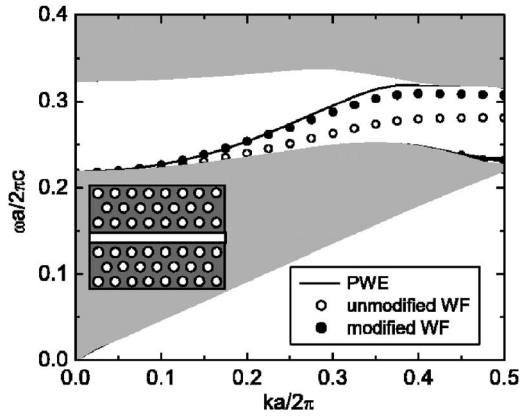

FIG. 7. Guided modes in the case of an air waveguide, of width $2R=0.58a$, in the triangular-lattice PC in the 2D TE mode. A solid line indicates the single guided mode calculated by the PWE method, and white and black points indicate those calculated by the unmodified optical WF method and modified optical WF method using the σ approximation, respectively. Shaded regions indicate the projected 2D photonic band structure. The inset indicates the structure of the air waveguide.

waves by the PWE method, and this structure has a 3D PBG of 17.7% We consider vector magnetic field MLWF's, and construct 12 localized basis functions: four MLWF's from the first four photonic bands below the 3D PBG, and eight maximally localized WF's from the tangle of crossing photonic bands above the 3D PBG. We can directly apply the MLWF method to the first four photonic bands below the 3D PBG. For the photonic bands above the 3D PBG, we construct eight pseudophotonic bands from the crossing photonic bands for $0.4 \leqslant \omega a/2\pi c \leqslant 0.65$ (outer frequency window). Then, we fix the photonic bands for $0.4 \leqslant \omega a/2\pi c \leqslant 0.48$ drawn by a dotted line (inner frequency window). This procedure is implemented through iterative calculations, and we take 1000 iterations (Appendix B). We take $20\times20\times20$ **k** points in the whole first BZ when constructing the MLWF's. Black points indicate the photonic band structure reproduced by the MLWF's. When reproducing the photonic band structure, we consider up to the fourth neighbor (separated by up to four lattice constants) interactions. As shown in Fig. 8, the solid lines and the black points coincide below the dotted line. However, they are very different above the dotted line.

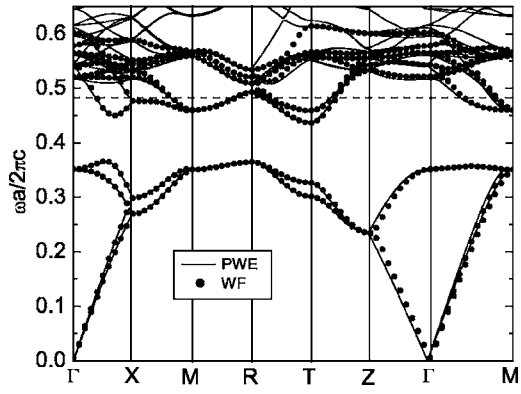

FIG. 8. Photonic band structure of a 3D PBG Si woodpile structure. The dielectric index of the Si woodpile is $\epsilon=11.9$ and the width and height of rods are chosen to be $d=0.25a$ and $h=0.3a$, respectively, where a is the distance between neighboring rods. Since one unit cell of the woodpile has four stacking layers, the periodicity of stacking layers is $c=4h=1.2a$. We consider the simple cubic structure $a\times a\times c$ as a unit cell. Solid lines indicate the photonic band structure calculated by the PWE method, and black points indicate that reproduced by the MLWF's. The solid lines and the black points coincide below the dotted line ($\omega a/2\pi c=0.48$). However, they are very different above the dotted line.

In Fig. 9, we show the absolute values of the first, second, seventh, and eighth, MLWF's of magnetic fields. Upper and lower figures of each MLWF indicate the distributions in the yz and xz planes, respectively. The 1st–8th, 11th–13th, and 17th Γ point distributions are chosen as the 1st–12th initial trial WF's, respectively. In this case, iterations converge. As shown in Fig. 8, double degeneracy appears at the Γ point in photonic band structures. In the Γ-point distributions that we use, the $(2n-1)$th and $2n$th $(n=1,2,3,4)$, and the eleventh and twelfth Γ-point distributions are doubly degenerate. Although Γ-point distributions should exhibit some of the symmetries of the photonic crystal, this symmetry is easily obscured when two Γ-point distributions are mixed due to double degeneracy. Our method for obtaining symmetric Γ-point distributions in the presence of degeneracy is discussed in Appendix C.

We set up the center points of the 1st–12th initial trial WF's at $(0,0,c/2)$, $(0,0,0)$, $(0,0,0)$, $(0,0,0)$, $(0.5a,0.5a,0)$, $(0.5a,0.5a,0)$, $(0,0,0)$, $(0,0,0)$, $(0.5a,0,0)$, $(0,0.5a,0)$, $(0,0,0)$, and $(0,0,0)$, respectively. In Eq. (42), we change $\exp[-(\mathbf{r}-\mathbf{r}^{(n)})^2/\sigma^2]$ to $\exp[-(x-x^{(n)})^2/\sigma_x^2]\exp[-(y-y^{(n)})^2/\sigma_y^2]\exp[-(z-z^{(n)})^2/\sigma_z^2]$ for all initial trial WF's, and guess $\sigma_x=\sigma_y=0.3a$, and $\sigma_z=0.8c$. The $(2n-1)$th and $2n$th $(n=2,3,4,5)$ MLWF's are related to each other by $|\mathbf{W}^{(\mathbf{H})}_{2n-1,0}\times(x,y,z)|=|\mathbf{W}^{(\mathbf{H})}_{2n,\mathbf{0}}(y,x,-z)|$. This follows from the corresponding relation between the Γ-point distributions. The first and second Γ-point distributions have an arbitrariness of polarization vectors at $\mathbf{k}=\mathbf{0}$ and $\omega a/2\pi c=0$. Details of choosing the polarization vectors are discussed in Appendix D.

We consider guided modes in the PBG resulting from the removal of one rod in the x-y plane. In this case, we must use the modified WF method since the defect modifies the surface polarization from charges. We consider overlap integrals of MLWF's separated by up to two unit cells in the calculation of the guided modes by the optical WF method. Figures 10(a)–10(c) show the guided modes in the unmodified optical WF method and the modified optical WF method without and with the σ approximation (Appendix A), respectively. Solid lines indicate the guided modes calculated by the PWE method in a supercell of $1\times4\times4$ unit cells. Shaded regions indicate the projected 3D photonic band structure. Black points indicate the guided modes calculated by the optical WF method. In Fig. 10(a), the PWE and unmodified optical WF methods do not coincide at all. In Fig. 10(b), there exist errors between the PWE and modified optical WF methods, although the modified WF method without using the σ approximation becomes close to the PWE method. In Fig.

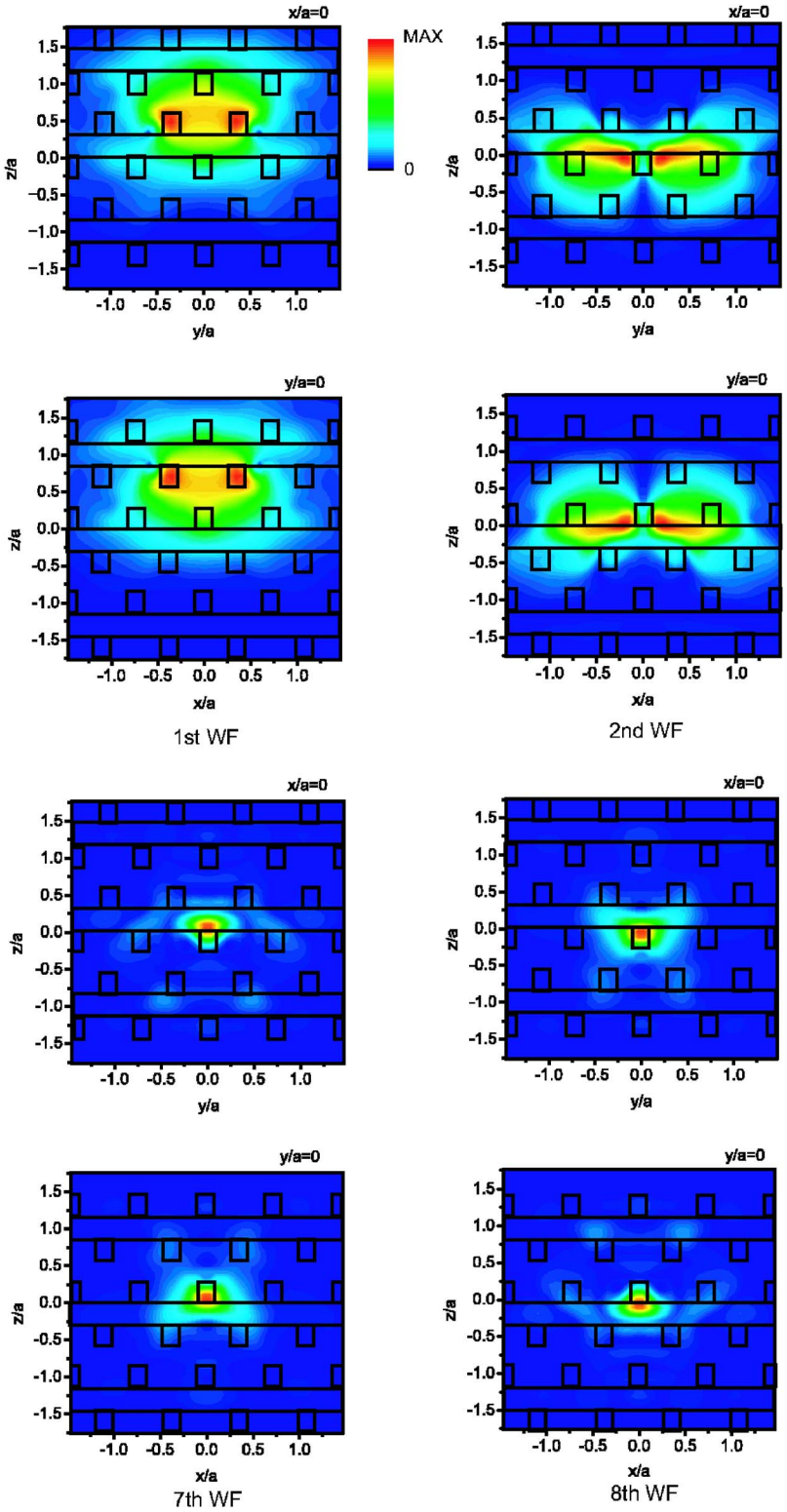

FIG. 9. (Color online) Absolute values of the first, second, seventh, and eighth MLWF's of magnetic fields in the 3D PBG Si woodpile structure. Upper and lower figures of each WF indicate the distributions in the yz and xz planes, respectively. The $(2n-1)$th and $2n$th $(n=2,3,4,5)$ MLWF's are related to each other by $|\mathbf{W}^{(\mathbf{H})}_{2n-1,\mathbf{0}}(x,y,z)|=|\mathbf{W}^{(\mathbf{H})}_{2n,\mathbf{0}}(y,x,-z)|$. This follows from the corresponding relation between the Γ-point distributions.

10(c), the modified optical WF method using the σ-approximation coincides with the PWE method for $\omega a/2\pi c \leqslant 0.42$. In the case of a small number of 343 terms in the Fourier series representation, the σ approximation plays an important role in reducing errors caused by the Gibbs phenomenon. For $\omega a/2\pi c > 0.42$, however, the modified optical WF method overestimates the guided mode frequency. Higher accuracy in this spectral range requires the inclusion of more MLWF's above the 3D PBG, a task which is complicated due to the number of crossing (entangled) photonic bands (see Fig. 8).

We next consider guided modes in the z direction by removing a zig-zag pattern of vertically stacked rod segments (vertical waveguide).[24,25] Such waveguides have been suggested as broadband lossless chip-to-chip interconnects in a 3D integrated optical circuit.[24,25] Figure 11(a) shows the

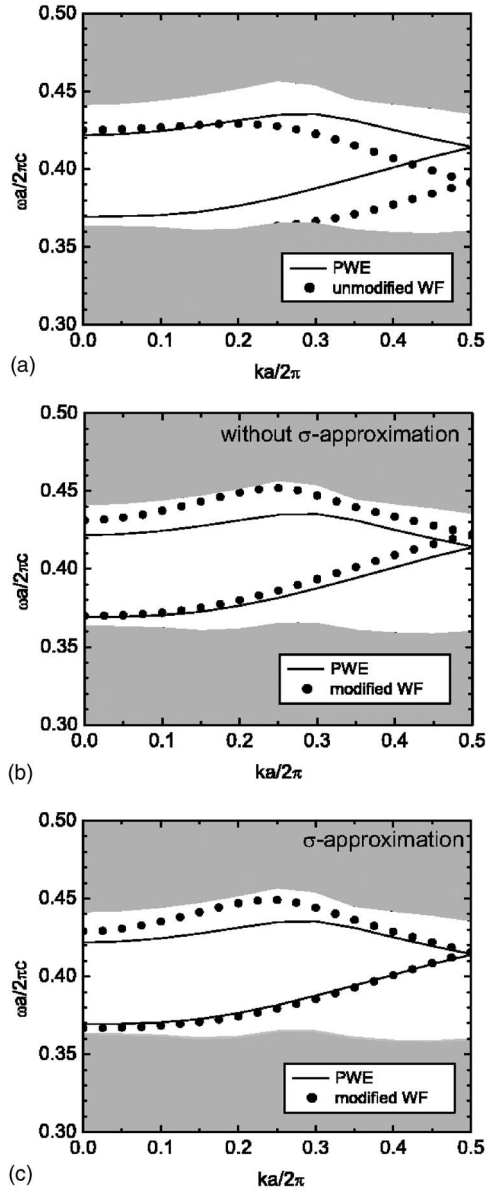

FIG. 10. Guided modes in the case of removing one rod in the 3D PBG Si woodpile structure: (a) unmodified optical WF method, (b) modified optical WF method without using the σ approximation and (c) modified optical WF method using the σ approximation. Solid lines and black points indicate the guided modes calculated by the PWE and optical WF methods, respectively. Shaded regions indicate the projected 3D photonic band structure.

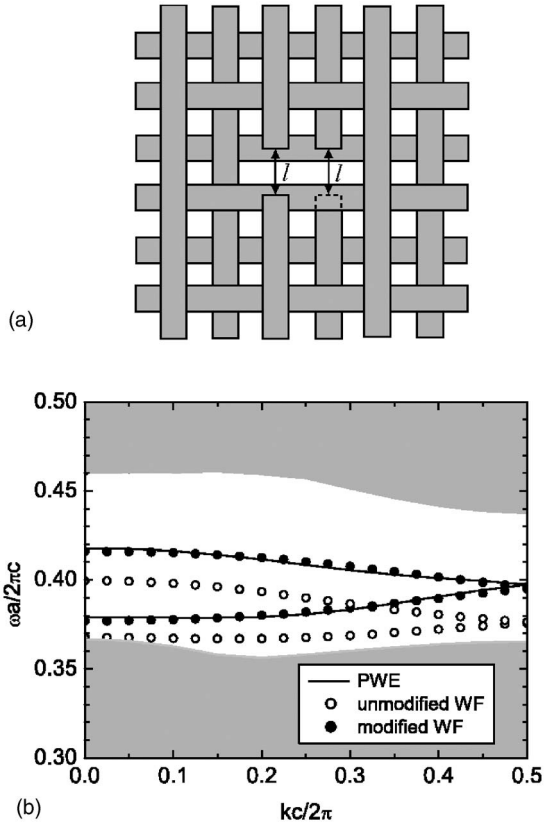

FIG. 11. (a) Structure of the defect in the 3D PBG Si woodpile structure. $l=0.5a$ is taken as the length of removed rod segments in the second and fourth layers from the bottom. (b) Guided modes in the case of removing rods segments in the vertically stacked direction in the 3D PBG Si woodpile structure. Solid lines indicate the guided modes calculated by the PWE method, and white and black points indicate those calculated by the unmodified optical WF method and modified optical WF method using the σ approximation, respectively. Shaded regions indicate the projected 3D photonic band structure.

structure of the defect, and $l=0.5a$ is taken as the length of removed rod segments in the second and fourth layers from the bottom. Figure 11(b) shows the guided modes in the optical WF method. Solid lines indicate the guided modes calculated by the PWE method in a supercell of $1\times4\times4$ cells. Shaded regions indicate the projected 3D photonic band structure. White and black points indicate the guided modes calculated by the unmodified optical WF method and the modified optical WF method using the σ approximation, respectively. In Fig. 11(b), the modified optical WF can recapture the guided mode precisely. The modified optical WF method improves accuracies greatly, compared to the unmodified optical WF.

In order to obtain highly accurate MLWF's, we typically calculate Bloch modes at 4000 **k** points in one-half of the first BZ. From these, we calculate the unitary transformation that provides MLWF's from the initial trial WF's. This process takes approximately 18 hours on a machine with three CPU's (one CPU is Alpha 2.5 GHz) and 10 GB memories. It requires an additional 6 hours to construct modified electric field WF's that take into account surface polarization charges. Once these WF's are calculated and stored, a variety of different photonic crystal circuit calculations can be performed rapidly.

It takes approximately 7 hours to calculate guided modes at one **k** point with 4375 plane waves by the PWE method in a supercell of $1\times4\times4$ unit cells, on the machine described above. In the optical WF method, on the other hand, it takes approximately 20 minutes to calculate overlap matrix elements in Eq. (19), once we obtain MLWF's. It is possible to calculate the guided modes at 21 **k** points in approximately 1 minute by using these overlap matrix elements. In other

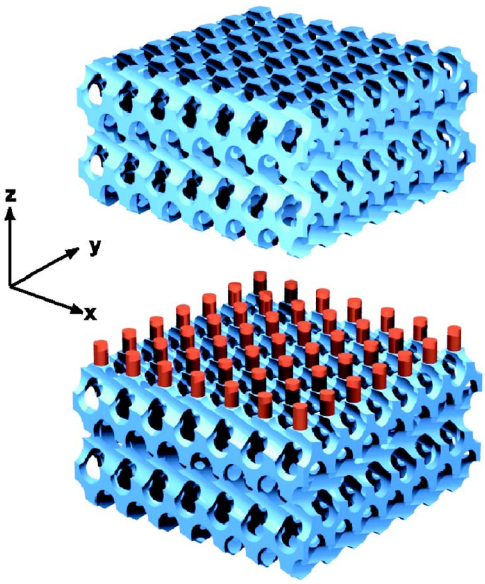

FIG. 12. (Color online) 2D-3D PBG heterostructure composed of inverse [001]-diamond:5 square spiral structures intercalated with a 2D microchip layer consisting of circular rods. The inverse square spiral structure is made from an air coil with a single loop. The dielectric index of a background Si is $\epsilon=11.9$. The [001]-diamond:5 has $[L,c,r]=[1.5,1.7,0.33]a$, where L, c, r, and a are the transverse arm length, the vertical period, the radius of coated coils, and the lattice constant, respectively. The 2D microchip layer is parallel to the 2D xy plane, and is sandwiched with the square spiral structures in the z direction. The radius of rods in the 2D microchip layer is $r_d=0.17a$ to fit the dielectric area, and the thickness of the 2D microchip layer is $t=0.5a$. In the calculation of the 2D-3D PBG heterostructure, we take 4 unit cells of the inverse [001]-diamond:5 square spiral structures in the z direction, based on the supercell technique. The overall length of a supercell is $L=4c+t=7.3a$.

words, the 3D optical WF method reduces the computational time relative to the PWE method by roughly two orders of magnitude, after the initial investment of time to construct accurate MLWF's.

D. 2D-3D PBG heterostructures

1. Inverse square spiral

To further illustrate the general applicability of the localized-light-orbital method, we consider a complex architecture consisting of a 3D PC consisting of air spirals in a silicon background and a thin square-lattice optical microchip layer intercalated within the 3D PBG cladding material. In Fig. 12, we show the 2D-3D PBG heterostructure composed of inverse [001]-diamond:5 square spiral structures inserted with a 2D microchip layer with circular rods.[5,6] The inverse square spiral structure is made from an air coil with a single loop. The dielectric index of a background Si is $\epsilon=11.9$. The [001]-diamond:5 has $[L,c,r]=[1.5,1.7,0.33]a$, where L, c, r, and a are the transverse arm length, the vertical period, the radius of coated coils and the lattice constant, respectively. The 2D microchip layer is parallel to the 2D xy plane, and is sandwiched with the square spiral structures in the z direction. The radius $r=0.33a$ of air spiral yields a dielectric area $(a-2r)\times(a-2r)=0.34a\times0.34a$ in a unit cell. The radius of rods in the 2D microchip layer is $r_d=0.17a$ to fit the dielectric area, and the thickness of the 2D microchip layer is $t=0.5a$. In the calculation of the 2D-3D PBG heterostructure, we take 4 unit cells of the inverse [001]-diamond:5 square spiral structures in the z direction, based on the supercell technique. The overall length of a supercell is $L=4c+t=7.3a$.

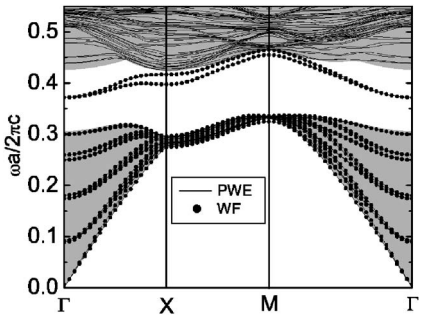

FIG. 13. Photonic band structure of the 2D-3D PBG heterostructure of Fig. 12 composed of inverse [001]-diamond:5 square spiral structures intercalated with a 2D microchip layer with circular rods. Solid lines indicate the photonic band structure calculated by the PWE method, and black points indicate that reproduced by the MLWF's. Shaded regions indicate the photonic band structure of the inverse square spiral projected to the 2D $\mathbf{k}_\parallel$ space.

Figure 13 shows the photonic band structure of the 2D-3D PBG heterostructure. Solid lines indicate the photonic band structure calculated with 1225 plane waves by the PWE method. Shaded regions indicate the 3D photonic band structure of the square spiral structure projected to the 2D $\mathbf{k}_\parallel$ space. In the region of frequencies and wave vectors between the lower and upper shaded regions, there are two planar guided photonic bands in which electromagnetic fields are localized around the 2D microchip layer. In our supercell construction, there are 16 photonic bands below the PBG, and many crossing photonic bands above the PBG. We construct 18 MLWF's: 16 MLWF's from below the PBG and two MLWF's from the entangled photonic bands above the PBG. We directly apply the MLWF method to the first 16 photonic bands below the PBG. For the photonic bands above the PBG, we construct two pseudophotonic bands from the crossing photonic bands for $0.35\leqslant\omega a/2\pi c\leqslant\omega_{19\mathbf{k}}a/2\pi c+0.045$ ($\mathbf{k}$-dependent outer frequency window). This outer frequency window extends $2\pi c/a\times0.045$ above the top of the 19th photonic band $\omega_{19\mathbf{k}}$. Then, we fix the planar guided photonic bands within the PBG of the spiral: $0.35\leqslant\omega a/2\pi c\leqslant\omega_{\mathrm{in},\mathbf{k}}a/2\pi c$ ($\mathbf{k}$-dependent inner frequency window). $\omega_{\mathrm{in},\mathbf{k}}$ is the lowest frequency of upper shaded regions at each $\mathbf{k}$ point. Electric field MLWF's are obtained using 1500 iterations (Appendix B). We take $40\times40\mathbf{k}_\parallel$ points in the whole first BZ when constructing the MLWF's. Black points indicate the photonic band structure reproduced by the MLWF's. When reproducing the photonic band structure, we consider up to the fourth neighbor (separated by up to four lattice constants) interactions. As shown in Fig. 13, the solid lines and the black points coincide in the

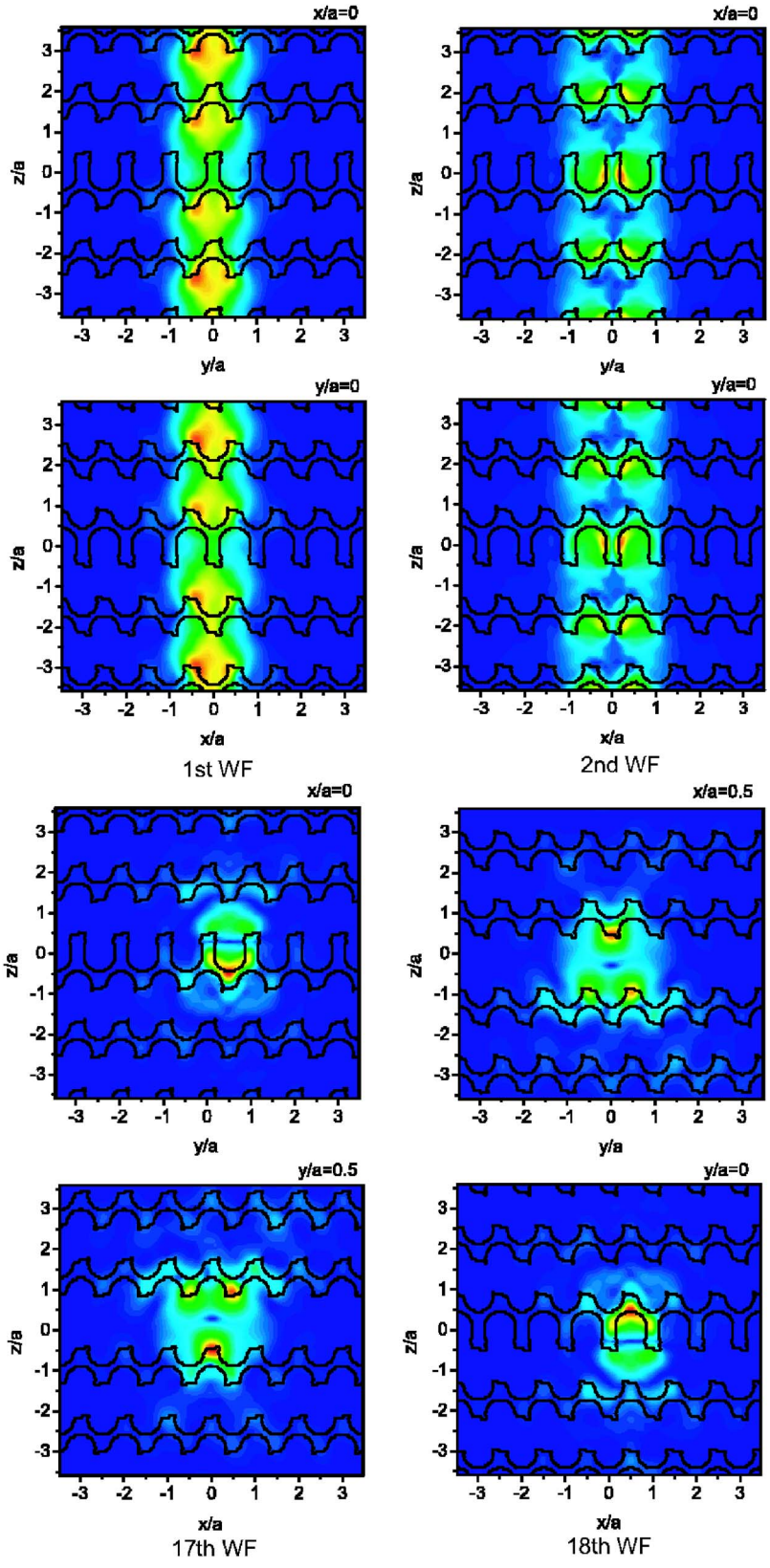

FIG. 14. (Color online) Absolute values of the first, second, seventeenth, and eighteenth ML-WF's of magnetic fields in the 2D-3D PBG heterostructure composed of inverse [001]-diamond:5 square spiral structures inserted with a 2D microchip layer with circular rods. Color patterns are the same as those in Fig. 9. Upper and lower figures of each WF indicate the distributions in the yz and xz planes, respectively. The $(2n-1)$th and $2n$th$(n \geqslant 2)$ WF's are related to each other by the symmetry: $|\mathbf{W}^{(\mathbf{H})}_{2n-1,\mathbf{0}_\parallel}(x,y,z)| = |\mathbf{W}^{(\mathbf{H})}_{2n,\mathbf{0}_\parallel}(y,x,-z)|$, following the corresponding relation between the respective Γ-point distributions.

first 16 photonic bands and within the inner frequency window.

In Fig. 14, we show the absolute values of the first, second, seventeenth, and eighteenth MLWF's of magnetic fields. Upper and lower figures of each MLWF indicate the distributions in the yz and xz planes, respectively. Color patterns are the same as those in Fig. 9. The 2D microchip layer is at $|z| \leqslant 0.25a$. The 1st–18th Γ-point distributions are used as the 1st–18th initial trial WF's, respectively. Details of obtaining symmetric Γ-point distributions are discussed in Appen-

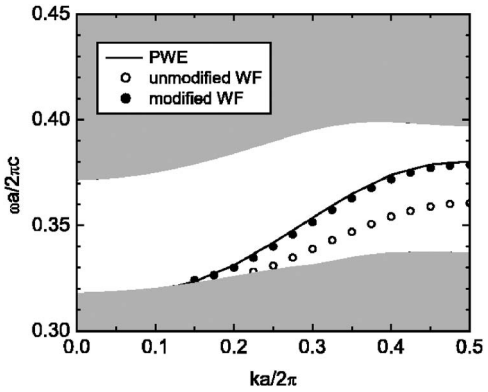

FIG. 15. Single guided mode in the case of removing one line of rods in the 2D microchip layer of the 2D-3D PBG heterostructure composed of inverse [001]-diamond:5 square spiral structures inserted with a 2D microchip layer with circular rods. A solid line indicates the single guided mode calculated by the PWE method, and white and black points indicate those calculated by the unmodified optical WF method and modified optical WF method using the σ approximation, respectively. Shaded regions indicate the projected 2D-3D photonic band structure.

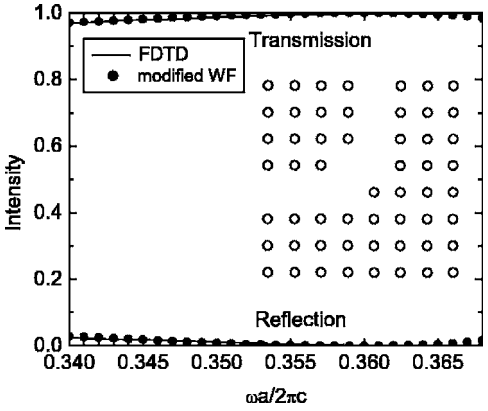

FIG. 16. Transmission and reflection spectra in a 90° bent air waveguide in the 2D microchip layer of the 2D-3D PBG heterostructure composed of inverse [001]-diamond:5 square spiral structures inserted with a 2D microchip layer with circular rods. Solid lines indicate the transmission and reflection spectra calculated by the FDTD method, and black points indicate those calculated by the modified optical WF method. The inset indicates the architecture of the 90° bent air waveguide.

dix C. We set up the center points of the 1st–16th initial trial WF's at (0,0), (0,0), $(0.5a,0)$, $(0,0.5a)$, $(0,0.5a)$, $(0.5a,0)$, $(0,0.5a)$, $(0.5a,0)$, $(0.5a,0)$, $(0,0.5a)$, $(0.5a,0.5a)$, $(0.5a,0.5a)$, (0,0), (0,0), (0,0), and (0,0), respectively. When constructing the pseudophotonic bands above the PBG, we started with the center points of the seventeenth and eighteenth initial trial WF's at $(0.5a,0.5a)$, $(0.5a,0.5a)$, respectively. However, the center points of the seventeenth and eighteenth MLWF's become $(0,0.5a)$ and $(0.5a,0)$, respectively, after iterative calculations. In Eq. (71), we take $\sigma=0.3a$. The $(2n-1)$th and $2n$th $(n\geq 2)$ WF's are related to each other by the symmetry, $|\mathbf{W}^{(\mathbf{H})}_{2n-1,\mathbf{0}_\parallel}(x,y,z)|=|\mathbf{W}^{(\mathbf{H})}_{2n,\mathbf{0}_\parallel}(y,x,-z)|$, following the corresponding relation between the respective Γ-point distributions. However, the first and second MLWF's are not related in this way because the first and second Γ-point distributions have an arbitrariness of polarization vectors at $\mathbf{k}_\parallel=\mathbf{0}_\parallel$ and $\omega a/2\pi c=0$ (Appendix D). Generally, WF's in 2D-3D PBG heterostructures are localized only in the 2D xy plane, and are not localized in the z direction. However, the seventeenth and eighteenth MLWF's are localized around the 2D microchip layer. This is because the seventeenth and eighteenth Γ-point distributions corresponding to planar guided modes.

We consider a guided mode in the case of removing one line of rods in the 2D microchip layer. We consider up to the third neighbor (separated by up to three lattice constants) interactions in the calculation of the guided mode by the optical WF method. Figure 15 shows the single guided mode in the optical WF method. A solid line indicates the single guided mode calculated by the PWE method. Shaded regions indicate the projected 2D-3D photonic band structure. White and black points indicate the single guided mode calculated by the unmodified optical WF method and the modified optical WF method using the σ approximation, respectively. Clearly the proper treatment of surface polarization charges is crucial to obtaining an accurate result.

Light propagation in PC circuits is often analyzed by the FDTD method. However, the optical WF method can also be applied to the analysis of optical transmission through PC circuits. In the 2D-3D PBG heterostructure, we calculate the light propagation through a sharp 90° bend in an air waveguide in the 2D microchip layer, comparing both the FDTD method and the modified optical WF method. We consider up to the third neighbor (separated by up to three lattice constants) interactions in the constructing the tight-binding wave equation using MLWF's. Figure 16 shows the transmission and reflection spectra in the 90° bent waveguide in the frequency range of $0.34\leq\omega a/2\pi c\leq 0.368$. Transmission and reflection coefficients are defined in the standard way.[12,29] Solid lines indicate results of the FDTD method and black points indicate the transmission and reflection spectra calculated by the modified optical WF method. Clearly, we can accurately recapture the transmission results of FDTD using the optical WF method. In the FDTD method, the resolution is 10 grid points per lattice constant, and it takes approximately 36 hours to calculate the transmission and reflection spectra over the stated frequency range. On the other hand, it takes approximately 10 minutes to calculate overlap matrix elements in Eq. (63) from the underlying MLWF's. We then obtain transmission at 29 frequency points within 150 minutes by using these overlap matrix elements. Clearly, the optical WF method offers considerable efficiency compared to the FDTD method. This efficiency is even more apparent when the circuit path becomes longer and more complicated.

2. Woodpile

In Fig. 17, we show another type of 2D-3D PBG heterostructure composed of 3D Si woodpiles intercalated with a 2D microchip layer consisting of a square lattice of square rods. We use the same Si woodpiles as discussed in Sec. IV C. The 2D microchip layer is parallel to the 2D xy plane,

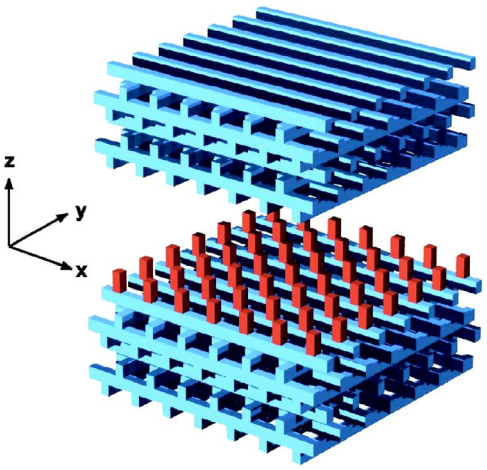

FIG. 17. (Color online) 2D-3D PBG heterostructure composed of 3D Si woodpiles intercalated with a 2D microchip layer consisting of a square lattice of square rods. We use the same Si woodpiles as discussed in Sec. IV C. The 2D microchip layer is parallel to the 2D xy plane, and is sandwiched by woodpiles above and below. The square rods in the 2D microchip layer are chosen to structurally match with the woodpiles, and the thickness of the 2D microchip layer is $t=0.8a$. In the calculation of the 2D-3D PBG heterostructure, we take 4 unit cells of the woodpile in the z direction, based on the supercell technique. The overall length of a supercell is $L=4c+t=5.6a$.

and is sandwiched by woodpiles above and below. The square rods in the 2D microchip layer are chosen to structurally match with the woodpiles, and the thickness of the 2D microchip layer is $t=0.8a$. This is a considerably thicker microchip layer than that considered for the spiral PBG heterostructure of the preceding section. As we will see, with such a large perturbation on the 3D bulk crystal, a large number of WF's become necessary to achieve high accuracy, especially in the frequency range approaching the bulk 3D photonic bands. In the calculation of the 2D-3D PBG heterostructure, we take 4 unit cells of the woodpile in the z direction, based on the supercell technique. The overall length of a supercell is $L=4c+t=5.6a$.

Figure 18 shows the photonic band structure of the 2D-3D PBG heterostructure. Solid lines indicate the photonic band structure calculated with 1225 plane waves by the PWE method. Shaded regions indicate the 3D photonic band structure of the woodpile projected to the 2D $\mathbf{k}_\parallel$ space. In the region of frequencies and wave vectors between the lower and upper shaded regions, there are two planar guided photonic bands. The electromagnetic fields of these planar guided photonic bands are localized around the 2D microchip layer. There are 16 photonic bands below the PBG, and a dense tangle of photonic bands crossing above the PBG. We construct 18 MLWF's: 16 MLWF's from the first 16 photonic bands below the PBG and two MLWF's from the crossing photonic bands above the PBG. We can directly apply the MLWF method to the first 16 photonic bands below the PBG. For the photonic bands above the PBG, we construct two pseudophotonic bands from the crossing photonic bands for $0.38 \leqslant \omega a/2\pi c \leqslant \omega_{17\mathbf{k}} a/2\pi c + 0.07$ ($\mathbf{k}$-dependent outer frequency window). This outer frequency

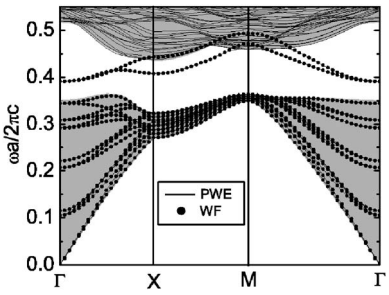

FIG. 18. Photonic band structure of the 2D-3D PBG heterostructure composed of 3D Si woodpiles intercalated with a 2D microchip layer consisting of a square lattice of square rods. Solid lines indicate the photonic band structure calculated by the PWE method, and black points indicate that reproduced by the MLWF's. Shaded regions indicate the photonic band structure of the woodpile projected to the 2D $\mathbf{k}_\parallel$ space.

window extends $2\pi c/a \times 0.07$ above the top of the 17th photonic band $\omega_{17\mathbf{k}}$. Then, we fix the planar guided photonic bands within the PBG of the woodpile: $0.38 \leqslant \omega a/2\pi c \leqslant \omega_{\text{in},\mathbf{k}} a/2\pi c$ ($\mathbf{k}$-dependent inner frequency window). $\omega_{\text{in},\mathbf{k}}$ is the lowest frequency of upper shaded regions at each $\mathbf{k}$ point. In this case, MLWF's are determined using 5000 iterations (Appendix B) 40×40 $\mathbf{k}_\parallel$ points in the whole first BZ when constructing the MLWF's. Black points indicate the photonic band structure reproduced by the MLWF's. When constructing the tight-binding wave equation, we consider up to the fourth neighbor (separated by up to four lattice constants) interactions. As shown in Fig. 18, the solid lines and the black points coincide in the first 16 photonic bands and within the inner frequency window.

In Fig. 19, we show the absolute values of the first, second, seventeenth, and eighteenth MLWF's of magnetic fields. Upper and lower figures of each MLWF indicate the distributions in the yz and xz planes, respectively. Color patterns are the same as those in Fig. 9. The 2D microchip layer is at $|z| \leqslant 0.4a$. The 1st–18th Γ-point distributions are used as the 1st–18th initial trial WF's, respectively. Details of obtaining symmetric Γ-point distributions are discussed in Appendix C. We set up the center points of the 1st–16th initial trial WF's at $(0,0)$, $(0,0)$, $(0.5a,0.5a)$, $(0.5a,0.5a)$, $(0.5a,0)$, $(0,0.5a)$, $(0,0.5a)$, $(0.5a,0)$, $(0.5a,0)$, $(0,0.5a)$, $(0,0)$, $(0,0)$, $(0,0.5a)$, $(0.5a,0)$, $(0,0)$, and $(0,0)$, respectively. When constructing the pseudophotonic bands above the PBG, we set up the center points of the seventeenth and eighteenth initial trial WF's at $(0.5a,0)$, $(0,0.5a)$, respectively. When constructing the MLWF's, on the other hand, we set up the center points of the seventeenth and eighteenth initial trial WF's at $(0.5a,0.5a)$, $(0.5a,0.5a)$, respectively. However, the center points of the seventeenth and eighteenth WF's become $(0,0.5a)$ and $(0.5a,0)$, respectively, after iterative calculations. In Eq. (71), we take $\sigma=0.3a$. The $(2n-1)$th and $2n$th $(n \geqslant 2)$ WF's are related to each other by the symmetry: $|\mathbf{W}^{(\mathbf{H})}_{2n-1,\mathbf{0}_\parallel}(x,y,z)| = |\mathbf{W}^{(\mathbf{H})}_{2n,\mathbf{0}_\parallel}(y,x,-z)|$, since the corresponding Γ-point distributions satisfy the same symmetry. However, the first and second MLWF's are not symmetric counterparts in this manner, since the first and second Γ-point distributions have an arbitrariness of polarization vectors at $\mathbf{k}_\parallel = \mathbf{0}_\parallel$

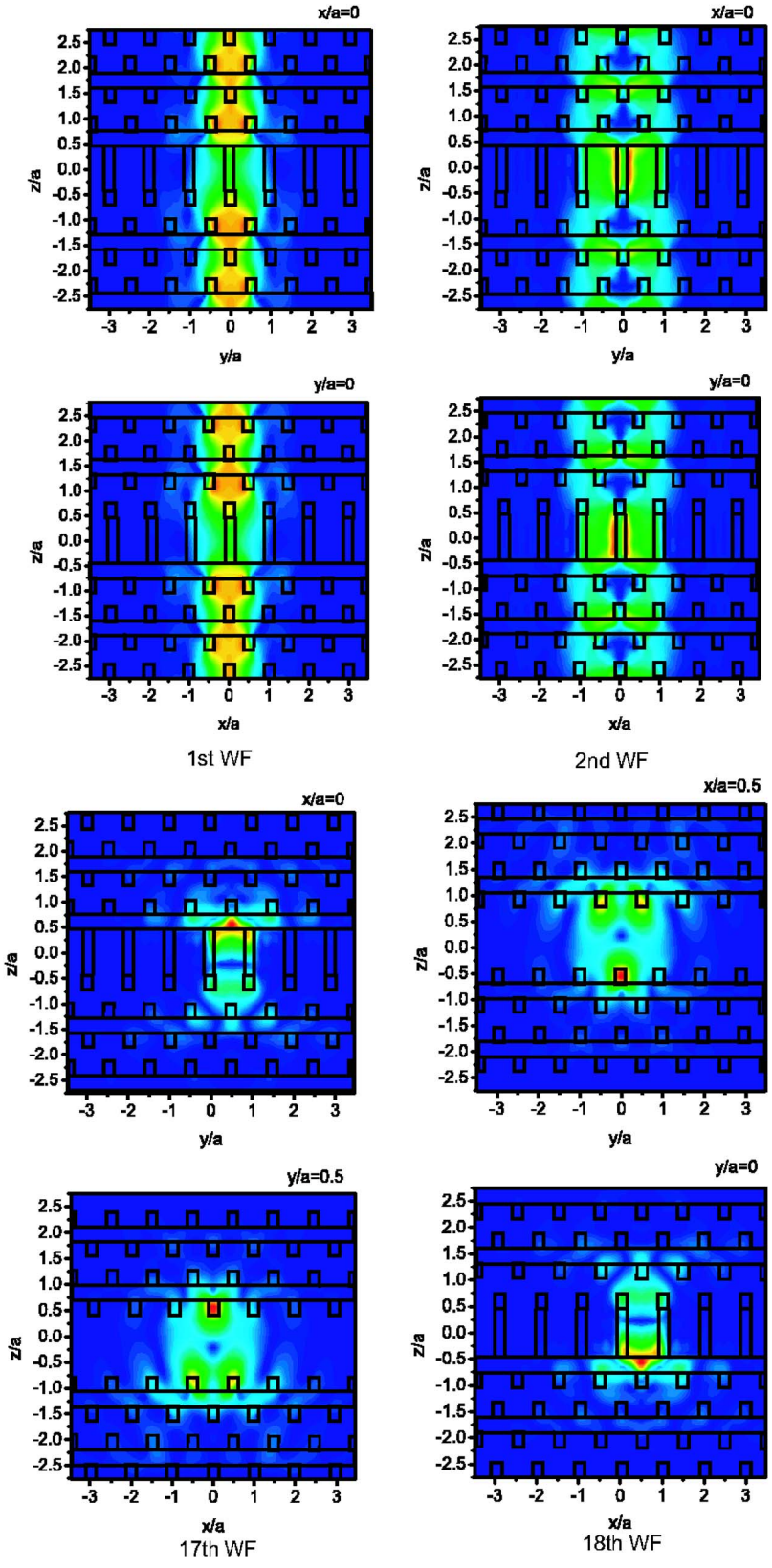

FIG. 19. (Color online) Absolute values of the first, second, seventeenth, and eighteenth MLWF's of magnetic fields in the 2D-3D PBG heterostructure composed of 3D Si woodpiles intercalated with a 2D microchip layer consisting of a square lattice of square rods. Color patterns are the same as those in Fig. 9. Upper and lower figures of each WF indicate the distributions in the yz and xz planes, respectively. The $(2n-1)$th and $2n$th$(n \geqslant 2)$ WF's are related to each other by the symmetry, $|\mathbf{W}^{(\mathbf{H})}_{2n-1,\mathbf{0}_\parallel}(x,y,z)| = |\mathbf{W}^{(\mathbf{H})}_{2n,\mathbf{0}_\parallel}(y,x,-z)|$, following the corresponding relation between the respective Γ-point distributions.

and $\omega a/2\pi c = 0$ (Appendix D). Generally, WF's in 2D-3D PBG heterostructures are localized only in the 2D xy plane, and are not localized in the z direction. However, the seventeenth and eighteenth MLWF's are localized around the 2D microchip layer. This is because the seventeenth and eighteenth Γ-point distributions represent planar guided bands and are localized around the 2D microchip layer.

We consider a guided mode in the case of removing one line of rods in the 2D microchip layer. We consider up to the third neighbor (separated by up to three lattice constants)

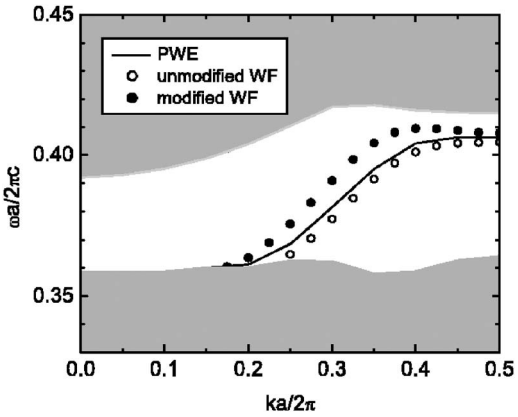

FIG. 20. Single guided mode in the case of removing one line of rods in the 2D microchip layer of the 2D-3D PBG heterostructure composed of 3D Si woodpiles intercalated with a 2D microchip layer consisting of a square lattice of square rods. A solid line indicates the single guided mode calculated by the PWE method, and white and black points indicate those calculated by the unmodified optical WF method and modified optical WF method using the σ approximation, respectively. Shaded regions indicate the projected 2D-3D photonic band structure.

interactions in the calculation of the guided mode by the optical WF method. Figure 20 shows the single guided mode in the optical WF method. In this case, the modified optical WF method, even in the σ approximation, deviates considerably from PWE. This is because planar guided photonic bands in Fig. 18 are strongly coupled to bulk 3D photonic bands above the PBG unlike those in Fig. 13. In other words, we must include more MLWF's above the PBG in order to obtain high accuracy.

E. 2D membrane photonic crystals

Unlike idealized 2D PC's, real 2D PC's exhibit broken translational symmetry in the third dimension. In a 2D membrane (thin slab), we consider the triangular-lattice PC composed of circular air holes in a 2D GaAs solid film of finite thickness. The background of the 2D membrane PC is the air. The dielectric index of the GaAs slab is $\epsilon=11.56$ and the radius of air holes is $R/a=0.29$, where a is the lattice constant. The thickness of the 2D membrane is $t=0.6a$. The overall length of a supercell with the 2D membrane and air cladding is chosen to be $L=4a$. As in the case of the microchip layer of Sec. IV D, we model the single 2D membrane starting from a periodically repeating set of membranes (in air) separated by a vertical spacing of $L=4a$. The properties of planar guided modes become insensitive of the choice of L for sufficiently large L. The 2D membrane is assumed to be parallel to the xy plane and symmetric at $z=0$. In 2D membrane PC's, there are even and odd modes. While in the even mode the z component of magnetic fields is even with respect to z, $H_z(\mathbf{r}_\parallel,z)=H_z(\mathbf{r}_\parallel,-z)$ [the parallel component of magnetic fields is odd, $\mathbf{H}_\parallel(\mathbf{r}_\parallel,z)=-\mathbf{H}_\parallel(\mathbf{r}_\parallel,-z)$], in the odd mode the z component of magnetic fields is odd with respect to z, $H_z(\mathbf{r}_\parallel,z)=-H_z(\mathbf{r}_\parallel,-z)$ [the parallel component of magnetic fields is even, $\mathbf{H}_\parallel(\mathbf{r}_\parallel,z)=\mathbf{H}_\parallel(\mathbf{r}_\parallel,-z)$]. The separation into

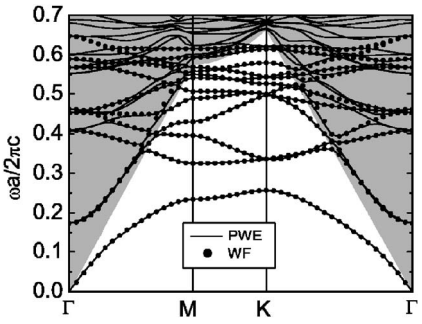

FIG. 21. Photonic band structure of the 2D membrane PC in the even mode. In a 2D membrane (thin slab), we consider the triangular-lattice PC composed of circular air holes in a 2D GaAs solid film of finite thickness. The background of the 2D membrane PC is the air. The dielectric index of the GaAs slab is $\epsilon=11.56$ and the radius of air holes is $R/a=0.29$, where a is the lattice constant. The thickness of the 2D membrane is $t=0.6a$. The overall length of a supercell with the 2D membrane and air cladding is chosen to be $L=4a$. Solid lines indicate the photonic band structure calculated by the PWE method, and black points indicate that reproduced by the MLWF's. Shaded regions indicate the light cone at $\omega \geqslant c|\mathbf{k}_\parallel|$.

even and odd modes can be determined by considering $\mathbf{h}^{(0)}_{n\mathbf{k}_\parallel}(\mathbf{G}_\parallel,G_z)$ in Eq. (47). While in the even mode $h^{(0)}_{zn\mathbf{k}_\parallel}(\mathbf{G}_\parallel,G_z)=h^{(0)}_{zn\mathbf{k}_\parallel}(\mathbf{G}_\parallel,-G_z)$ and $\mathbf{h}^{(0)}_{\parallel n\mathbf{k}_\parallel}(\mathbf{G}_\parallel,G_z)=-\mathbf{h}^{(0)}_{\parallel n\mathbf{k}_\parallel}(\mathbf{G}_\parallel,-G_z)$, in the odd mode $h^{(0)}_{zn\mathbf{k}_\parallel}(\mathbf{G}_\parallel,G_z)=-h^{(0)}_{zn\mathbf{k}_\parallel}(\mathbf{G}_\parallel,-G_z)$ and $\mathbf{h}^{(0)}_{\parallel n\mathbf{k}_\parallel}(\mathbf{G}_\parallel,G_z)=\mathbf{h}^{(0)}_{\parallel n\mathbf{k}_\parallel}(\mathbf{G}_\parallel,-G_z)$. Only light that satisfies the condition of total internal reflections is confined strictly to propagate within the 2D membrane PC's. The region of frequencies and wave vectors in which light leaks into external air background is called the light cone. In the 2D membrane PC's, the primary interest is in light outside the light cone, that is confined and guided. The 2D membrane PC described above has a large PBG in the even mode. However, this PBG is different from conventional PBG's because of the light cone. The even mode bears some similarity to the TE mode in idealized 2D PBG structures.

Figure 21 shows the photonic band structure of the 2D membrane PC in the even mode. Solid lines indicate the photonic band structure calculated with 1225 plane waves by the PWE method. Shaded regions indicate the light cone at $\omega \geqslant c|\mathbf{k}_\parallel|$. We construct 12 MLWF's from 12 lowest (crossing) photonic bands. This requires that we first construct 12 pseudophotonic bands from the crossing photonic bands for $0 \leqslant \omega a/2\pi c \leqslant 0.65$ (outer frequency window). We fix photonic bands for $0 \leqslant \omega a/2\pi c \leqslant 0.4$ inside the light cone and for $0 \leqslant \omega a/2\pi c \leqslant 0.51$ outside the light cone, respectively (inner frequency windows). This procedure is implemented through iterative calculations with 1000 iterations (Appendix B). We take 40×40 $\mathbf{k}_\parallel$ points in the whole first BZ when constructing the MLWF's. Black points indicate the photonic band structure reproduced by the MLWF's. When constructing the tight-binding wave equation, we consider up to the fourth neighbor (separated by up to four lattice constants) interactions. As shown in Fig. 21, the solid lines and the black points coincide within the inner frequency window.

In Fig. 22, we show the absolute values of the first, second, seventh, and eighth MLWF's of magnetic fields. Upper

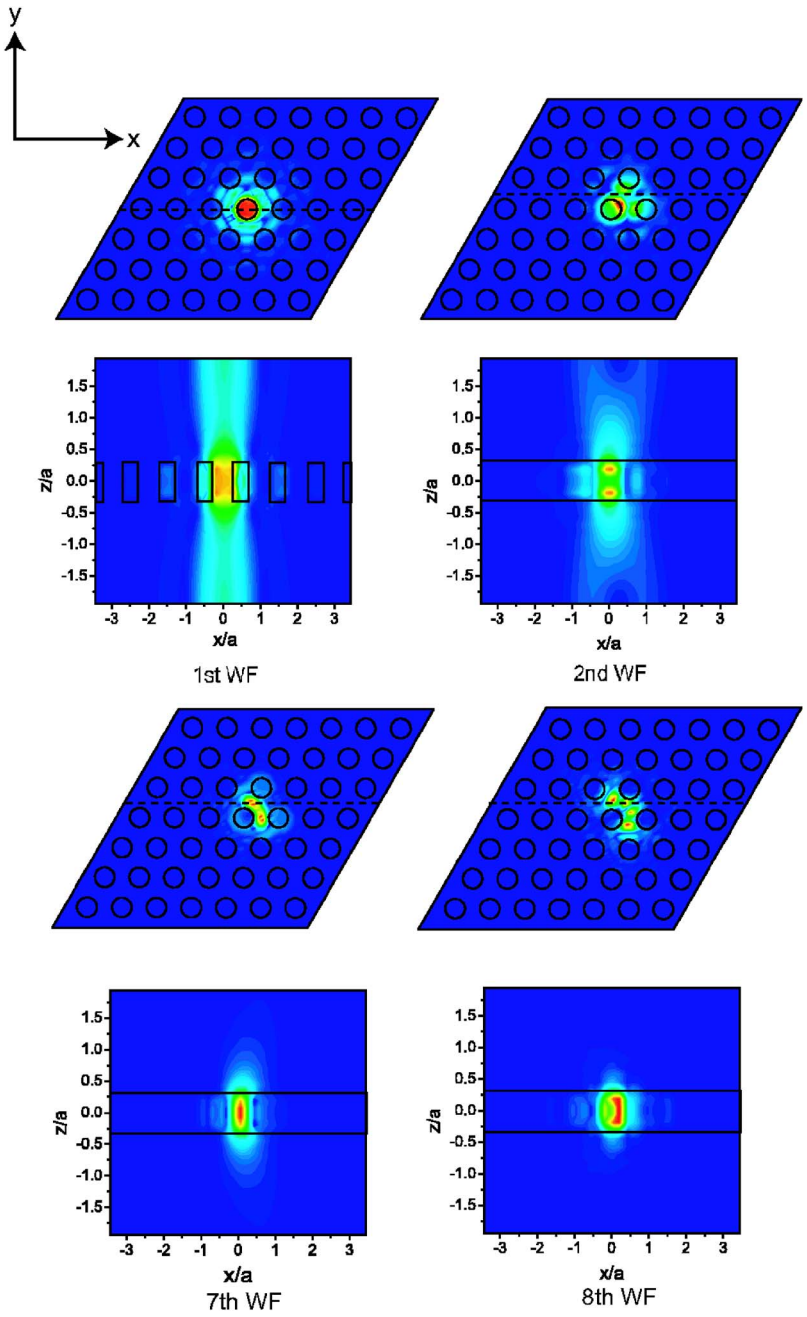

FIG. 22. (Color online) Absolute values of the first, second, seventh, and eighth MLWF's of magnetic fields in the 2D membrane PC in the even mode. Color patterns are the same as those in Fig. 9. Upper and lower figures of each MLWF indicate the distributions at $z=0$ and at a certain choice of y indicated by dotted lines in the upper figures, respectively.

and lower figures of each MLWF indicate the distributions at $z=0$ and at a certain choice of y indicated by dotted lines in the upper figures, respectively. Color patterns are the same as those in Fig. 9. When in each upper figure a center hole is placed at (0, 0), the dotted line of the first MLWF corresponds to $y=0$. The dotted lines of the second, seventh, and eighth MLWF's are $y=\sqrt{3}a/4$, which is one-half the height of the triangle composed of three air holes. The first, second, third, fourth, seventh, eighth, ninth, twelfth, thirteenth, fourteenth, seventeenth, and eighteenth Γ-point distributions are chosen as the 1st–12th initial trial WF's, respectively. In this case, iterations converge. Following the discussion of Sec. IV B, we place the center point of the first initial trial WF at (0, 0). Those of the 2nd–12th initial trial WF's are placed at $(a/2, \sqrt{3}a/6)$, the center of gravity of the triangle composed of three air holes. The center points of the converged MLWF's are generally different from those of the initial trial WF's. However, the center points of the MLWF's are still near $(a/2, \sqrt{3}a/6)$. In Eq. (71), we take $\sigma=0.3a$. The 1st–3rd MLWF's are not very well localized around the 2D membrane PC whereas others are relatively localized.

Finally, we consider guided modes in the case of one missing line of air holes (dielectric waveguide). The tight-binding wave equation is constructed keeping up to the third neighbor (separated by up to three lattice constants) overlap integrals between the modified MLWF's. Figures 23(a)–23(c) show the guided modes in the unmodified optical WF method and the modified optical WF method without and with the σ approximation, respectively. Solid lines indicate the guided modes calculated by the PWE method. Light and dark shaded regions indicate the projected photonic band structure of the 2D membrane PC and the light cone, respec-

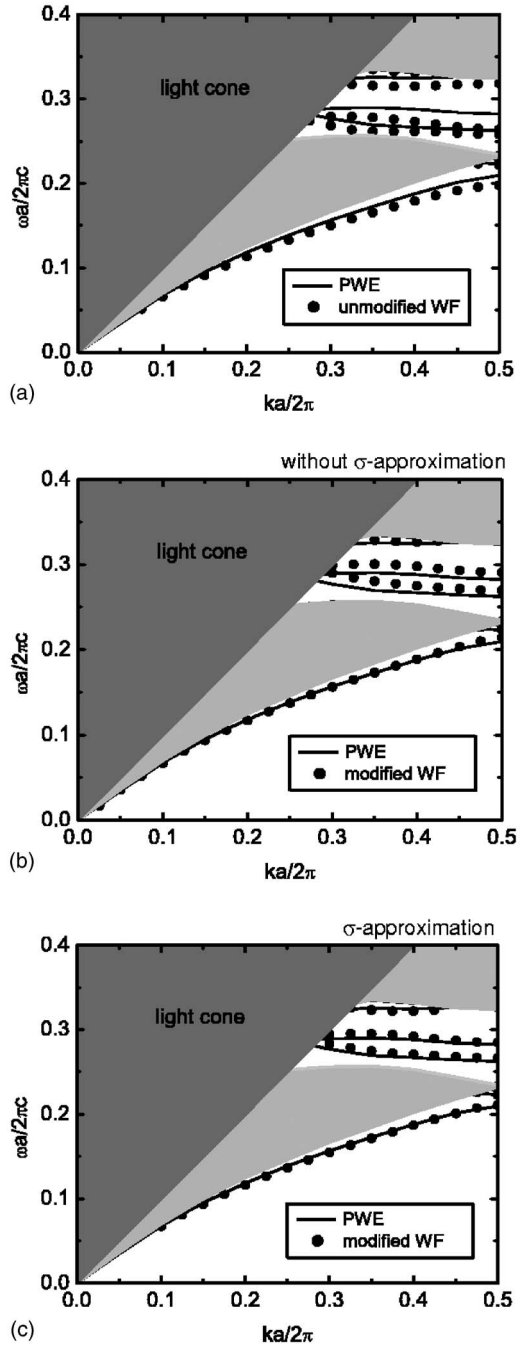

FIG. 23. Guided modes in the case of missing one line of air holes in the 2D membrane PC of Fig. 21 in the even mode: (a) unmodified optical WF method, (b) modified optical WF method without using the σ approximation and (c) modified optical WF method using the σ approximation. Solid lines indicate the guided modes calculated by the PWE method, and black points indicate those calculated by the optical WF method. Light and dark shaded regions indicate the projected photonic band structure of the 2D membrane PC and the light cone, respectively.

tively. Black points indicate the guided modes calculated by the optical WF method. In Fig. 23(a), when the redistribution of polarization charges is not properly treated, the solid lines and the black points do not coincide at all. In Fig. 23(b), there exist errors between the PWE and modified optical WF methods, although the modified WF method without using the σ approximation becomes close to the PWE method. In Fig. 23(c), however, the PWE and modified optical WF methods coincide.

V. CONCLUSIONS

In conclusion, we have demonstrated the broad applicability, precision, and efficiency of optical WF method to a variety of 2D and 3D periodic dielectric microstructures with planar, line, and point defects. As in the case of electronic systems,[27,28] MLWF's are defined by the unitary transformation that minimizes a wave function spread functional. By forming a basis of tightly localized orbitals of light, we can accurately recapture electromagnetic effects using a tight-binding wave equation involving overlap matrix elements within four or fewer neighboring unit cells. In general, when there is at least a small PBG (over all **k** points) between the Nth and $(N+1)$th bands, we construct N maximally localized WF's. In the case of crossing photonic bands, we first construct pseudophotonic bands from them. Γ-point distributions of the underlying Bloch functions are used for initializing shapes of localized light orbitals. In bulk 2D and 3D PBG structures MLWF's are localized in 2D and 3D spaces, respectively. But in 2D-3D PBG heterostructures and 2D membrane PC's they are localized only in the 2D xy plane and have periodicities in the z direction. A key insight in efficiently obtaining a precise description of electromagnetic flow in structures containing defects (deviations from periodicity) is the modification of MLWF's to accommodate the polarization charge densities created by the defects. This creates discontinuities in the electromagnetic field vectors, not previously encountered in electronic structure calculations or scalar wave calculations. By substituting the modified electric field into Maxwell's wave equation, we obtain a matrix equation that accurately describes electromagnetic flow through waveguides and point-defect modes as well as transmission and reflection of light within complex 3D PBG circuit paths. We find that, in general, the electric-field optical WF method is more accurate for the calculation of defect modes than the magnetic-field orbitals. For the TM mode in idealized 2D PBG structures, we do not have to modify the expansion representation of the electric field. This problem reduces to a scalar wave equation and we can obtain high accurate guided modes with a small number of WF's, as shown by previous authors.[12,13] For the TE mode in idealized 2D PBG structures, the accurate description of guided modes and other defects depends crucially on the use of modified optical WF's that account for the redistribution of induced polarization charges.

In bulk 3D PBG structures, 2D-3D PBG heterostructures and 2D membrane PC's, using less than twenty modified optical WF's and two orders of magnitude less computational time, we obtain high accuracies for guided modes. In contrast the PWE supercell methods require over 4000 basis states. Likewise in the calculation of transmission and reflection in 3D waveguide bends, we accurately recapture the results of FDTD with greatly reduced computational effort. These results suggest that 3D localized light orbitals provide

a reliable method for describing realistic electromagnetic effects in a variety of 3D PBG microchips. Moreover, the localized light orbital method is applicable to very large-scale optical circuits, where FDTD and plane wave expansion methods would be computationally prohibitive.

In addition to materials with a real, positive and frequency-independent dielectric function, the localized light orbital basis may provide a powerful tool for describing light propagation in metallic photonic crystals. Below the metallic plasma frequency, the dielectric constant is negative. This represents a "tunneling" region when the electromagnetic wave may decay exponentially. Since plane waves are inefficient in representing this effect, it typically requires a very large number of these extended basis functions to accurately represent strong exponential decay. MLWF's, on the other hand, are ideally suited to describe strong localization effects with a small number of basis states. The extension of the localized light orbital basis to PBG materials with nonlinear, complex, and frequency-dependent dielectric functions is a promising avenue for future research.

ACKNOWLEDGMENTS

The authors are grateful to Kurt Busch, Sergei F. Mingaleev, and Mathiass Schillinger for valuable discussions about the 2D optical WF method applied to TM modes. This work was supported in part by the Natural Sciences and Engineering Research Council of Canada, the Government of Ontario, and the Canadian Institute of Advanced Research.

APPENDIX A: SOLUTIONS OF THE POISSON EQUATION AND ELIMINATIONS OF THE GIBBS PHENOMENA

1. Bulk 2D and 3D PBG structures

In bulk 2D and 3D PBG structures, we need only calculate the scalar potential $\phi_{n\mathbf{R}}(\mathbf{r})$ inside defects, as shown in Eq. (22). For simplicity, we consider a hypothetical periodic dielectric $\tilde{\epsilon}(\mathbf{r}) \equiv \epsilon_p(\mathbf{r}) + \delta\epsilon_p(\mathbf{r})$, $\delta\epsilon_p(\mathbf{r}) \equiv \Sigma_{\mathbf{R}} \delta\epsilon(\mathbf{r}+\mathbf{R})$ when solving the Poisson equation

$$\nabla \cdot [\tilde{\epsilon}(\mathbf{r})\, \nabla\, \phi_{n\mathbf{R}}(\mathbf{r})] = \nabla \cdot [\delta\epsilon_p(\mathbf{r}) \mathbf{W}^{(\mathbf{E})}_{n\mathbf{R}}(\mathbf{r})]. \tag{A1}$$

The right-hand hand side of Eq. (A1) corresponds to a polarization charge created by $\delta\epsilon_p(\mathbf{r})$. $\delta\epsilon_p(\mathbf{r})\mathbf{W}^{(\mathbf{E})}_{n\mathbf{R}}(\mathbf{r})$ exhibits abrupt discontinuities because it vanishes outside defects. However, when representing discontinuities by a small number of terms in a Fourier series, oscillation errors called the Gibbs phenomena appear. Taking a divergence of such changes causes unexpected polarization charges that hinder high accuracies. We eliminate the Gibbs phenomenon by using a smoothing algorithm known as the σ approximation.[30] The relevant functions are given by

$$\tilde{\epsilon}(\mathbf{r}) = \sum_{\mathbf{G}} \tilde{\epsilon}(\mathbf{G}) \exp(i\mathbf{G} \cdot \mathbf{r}), \tag{A2}$$

$$\delta\epsilon_p(\mathbf{r}) = \sum_{\mathbf{G}} \delta\epsilon_p(\mathbf{G}) e^{i\mathbf{G}\cdot\mathbf{r}}, \tag{A3}$$

$$\phi_{n\mathbf{R}}(\mathbf{r}) = \frac{v}{(2\pi)^d} \int_{\mathrm{BZ}} d^d\mathbf{k} e^{-i\mathbf{k}\cdot\mathbf{R}} \sum_{\mathbf{G}} \phi_{n\mathbf{k}}(\mathbf{G}) e^{i(\mathbf{k}+\mathbf{G})\cdot\mathbf{r}}, \tag{A4}$$

and

$$\mathbf{W}^{(\mathbf{E})}_{n\mathbf{R}}(\mathbf{r}) = \frac{v}{(2\pi)^d} \int_{\mathrm{BZ}} d^d\mathbf{k} e^{-i\mathbf{k}\cdot\mathbf{R}} \sum_{\mathbf{G}} \mathbf{E}_{n\mathbf{k}}(\mathbf{G}) e^{i(\mathbf{k}+\mathbf{G})\cdot\mathbf{r}}, \tag{A5}$$

where $d(=2,3)$ is the dimension. Then,

$$\delta\epsilon_p(\mathbf{r})\mathbf{W}^{(\mathbf{E})}_{n\mathbf{R}}(\mathbf{r}) = \frac{v}{(2\pi)^d} \int_{\mathrm{BZ}} d^d\mathbf{k} e^{-i\mathbf{k}\cdot\mathbf{R}} \sum_{\mathbf{G}} \sum_{\mathbf{G}'} \sigma(\mathbf{G}) \times \delta\epsilon_p(\mathbf{G}-\mathbf{G}') \mathbf{E}_{n\mathbf{k}}(\mathbf{G}') e^{i(\mathbf{k}+\mathbf{G})\cdot\mathbf{r}}, \tag{A6}$$

where $\sigma(\mathbf{G})$ is inserted by hand to eliminate the Gibbs phenomenon.[30] For example, in 3D simple cubic structures $a \times a \times c$,

$$\sigma(\mathbf{G}) = \frac{\sin\{(G_x a)/[2(N_G+1)]\}}{(G_x a)/[2(N_G+1)]} \times \frac{\sin\{(G_y a)/[2(N_G+1)]\}}{(G_y a)/[2(N_G+1)]} \times \frac{\sin\{(G_z c)/[2(N_G+1)]\}}{(G_z c)/[2(N_G+1)]}, \tag{A7}$$

where $|G_x| \leq (2\pi/a)N_G$, $|G_y| \leq (2\pi/a)N_G$, and $|G_z| \leq (2\pi/c)N_G$ (N_G, integer). The number of 2D and 3D reciprocal lattice vectors is $(2N_G+1)^2$ and $(2N_G+1)^3$, respectively. In bulk 2D PBG structures, we take $N_G=10$. Here the Gibbs phenomenon is small because of the large number of terms in the expansion. In bulk 3D PBG structures, however, we take $N_G=3$. In this case, the Gibbs phenomenon is more significant and the σ-smoothing algorithm is crucial.

By substituting Eqs. (A2)–(A6) into Eq. (A1), we obtain a linear equation of $\phi_{n\mathbf{k}}(\mathbf{G})$,

$$\sum_{\mathbf{G}'} \tilde{\epsilon}(\mathbf{G}-\mathbf{G}')(\mathbf{k}+\mathbf{G}) \cdot (\mathbf{k}+\mathbf{G}') \phi_{n\mathbf{k}}(\mathbf{G}') = -i \sum_{\mathbf{G}'} \sigma(\mathbf{G}) \delta\epsilon_p(\mathbf{G}-\mathbf{G}')(\mathbf{k}+\mathbf{G}) \cdot \mathbf{E}_{n\mathbf{k}}(\mathbf{G}'). \tag{A8}$$

Solving (A8) for $\phi_{n\mathbf{k}}(\mathbf{G})$, we obtain the WF modification (A4).

2. 2D-3D PBG heterostructures and 2D membrane photonic crystals

In 2D-3D PBG heterostructures and 2D membrane photonic crystals, we consider a hypothetical periodic dielectric $\tilde{\epsilon}(\mathbf{r}_\parallel, z) \equiv \epsilon_p(\mathbf{r}_\parallel, z) + \delta\epsilon_p(\mathbf{r}_\parallel, z)$, $\delta\epsilon_p(\mathbf{r}_\parallel, z) \equiv \Sigma_{\mathbf{R}_\parallel} \delta\epsilon(\mathbf{r}_\parallel + \mathbf{R}_\parallel, z)$ when solving the Poisson equation,

$$\nabla \cdot \{\tilde{\epsilon}(\mathbf{r}_\parallel, z)\, \nabla\, \phi_{n\mathbf{R}_\parallel}(\mathbf{r}_\parallel, z)\} = \nabla \cdot \{\delta\epsilon_p(\mathbf{r}_\parallel, z) \mathbf{W}^{(\mathbf{E})}_{n\mathbf{R}_\parallel}(\mathbf{r}_\parallel, z)\}. \tag{A9}$$

The relevant functions are given by

$$\tilde{\epsilon}(\mathbf{r}_\parallel, z) = \sum_{\mathbf{G}_\parallel} \sum_{G_z} \tilde{\epsilon}(\mathbf{G}_\parallel, G_z) e^{i(\mathbf{G}_\parallel \cdot \mathbf{r}_\parallel + G_z z)}, \tag{A10}$$

$$\delta\epsilon_p(\mathbf{r}_\parallel,z)=\sum_{\mathbf{G}_\parallel}\sum_{G_z}\delta\epsilon_p(\mathbf{G}_\parallel,G_z)e^{i(\mathbf{G}_\parallel\cdot\mathbf{r}_\parallel+G_z z)}, \tag{A11}$$

$$\phi_{n\mathbf{R}_\parallel}(\mathbf{r}_\parallel,z)=\frac{v_{2D}}{(2\pi)^2}\int_{BZ}d^2\mathbf{k}_\parallel e^{-i\mathbf{k}_\parallel\cdot\mathbf{R}_\parallel}\times\sum_{\mathbf{G}_\parallel}\sum_{G_z}\phi_{n\mathbf{k}_\parallel}(\mathbf{G}_\parallel,G_z)e^{i[(\mathbf{k}_\parallel+\mathbf{G}_\parallel)\cdot\mathbf{r}_\parallel+G_z z]}, \tag{A12}$$

and

$$\mathbf{W}^{(\mathrm{E})}_{n\mathbf{R}_\parallel}(\mathbf{r}_\parallel,z)=\frac{v_{2D}}{(2\pi)^2}\int_{BZ}d^2\mathbf{k}_\parallel e^{-i\mathbf{k}_\parallel\cdot\mathbf{R}_\parallel}\times\sum_{\mathbf{G}_\parallel}\sum_{G_z}\mathbf{E}_{n\mathbf{k}_\parallel}(\mathbf{G}_\parallel,G_z)e^{i[(\mathbf{k}_\parallel+\mathbf{G}_\parallel)\cdot\mathbf{r}_\parallel+G_z z]}. \tag{A13}$$

We consider supercells of size $a\times a\times L$ where $L=Mc+t$, M is the number of 3D unit cells in a supercell, c is the vertical length of a 3D unit cell, and t is the thickness of a 2D microchip. In this case the smoothing factor is

$$\sigma(\mathbf{G}_\parallel,G_z)=\frac{\sin\{(G_x a)/[2(N_G+1)]\}}{(G_x a)/[2(N_G+1)]}\times\frac{\sin\{(G_y a)/[2(N_G+1)]\}}{(G_y a)/[2(N_G+1)]}\times\frac{\sin\{(G_z L)/[2M(N_G+1)]\}}{(G_z L)/[2M(N_G+1)]}, \tag{A14}$$

where $|G_x|\leqslant(2\pi/a)N_G$, $|G_y|\leqslant(2\pi/a)N_G$, and $|G_z|\leqslant(2\pi/L)MN_G$ (N_G, integer). The number of reciprocal lattice vectors is $(2N_G+1)^2(2MN_G+1)$ and we take $M=4$ and $N_G=3$. With such small $N_\mathbf{G}$, the Gibbs phenomenon is significant and the σ-smoothing algorithm is essential. By substituting Eqs. (A10)–(A13) into Eq. (A9), we obtain a linear equation of $\phi_{n\mathbf{k}_\parallel}(\mathbf{G}_\parallel,G_z)$,

$$\sum_{\mathbf{G}'_\parallel}\sum_{G'_z}\tilde{\epsilon}(\mathbf{G}_\parallel-\mathbf{G}'_\parallel,G_z-G'_z)(\mathbf{k}_\parallel+\mathbf{G})\cdot(\mathbf{k}_\parallel+\mathbf{G}')\phi_{n\mathbf{k}_\parallel}(\mathbf{G}'_\parallel,G'_z)=-i\sum_{\mathbf{G}'_\parallel}\sum_{G'_z}\sigma(\mathbf{G}_\parallel,G_z)\delta\epsilon_p(\mathbf{G}_\parallel-\mathbf{G}'_\parallel,G_z-G'_z)\times(\mathbf{k}_\parallel+\mathbf{G})\cdot\mathbf{E}_{n\mathbf{k}_\parallel}(\mathbf{G}'_\parallel,G'_z). \tag{A15}$$

Solving (A15) for $\phi_{n\mathbf{k}_\parallel}(\mathbf{G}_\parallel,G_z)$, we obtain the Coulomb potential of the defect surface polarization charge (A12).

APPENDIX B: OPTIMAL LOCALIZATION OF LIGHT ORBITALS AND EXTRACTION OF PSEUDOPHOTONIC BANDS

Adapting the methods introduced for electronic WF's,[27,28] we minimize the spread functional (30) and (67). First, we consider the case of $N_\mathbf{k}=N$ at all $\mathbf{k}$ points. Ω is represented as a $\mathbf{k}$ summation by a set of overlap matrices,

$$M^{(\mathbf{k},\mathbf{b})}_{mn}=\langle\mathbf{h}_{m\mathbf{k}}|\mathbf{h}_{n\mathbf{k}+\mathbf{b}}\rangle. \tag{B1}$$

By expanding the identity $\langle\mathbf{h}_{n\mathbf{k}+\mathbf{b}}|\mathbf{h}_{n\mathbf{k}+\mathbf{b}}\rangle=1$ order by order in b, we obtain an expansion of the form

$$M^{(\mathbf{k},\mathbf{b})}_{nn}=1+ixb+\tfrac{1}{2}yb^2+O(b^3), \tag{B2}$$

where x and y are real.

Then, Eqs. (31)–(34) are expressed as

$$\bar{\mathbf{r}}_n=-\frac{1}{N_{kp}}\sum_{\mathbf{k},\mathbf{b}}w_\mathbf{b}\mathbf{b}\,\mathrm{Im}(\ln M^{(\mathbf{k},\mathbf{b})}_{mn}), \tag{B3}$$

$$\langle r^2\rangle_n=\frac{1}{N_{kp}}\sum_{\mathbf{k},\mathbf{b}}w_\mathbf{b}\{(1-|M^{(\mathbf{k},\mathbf{b})_{nn}}|^2)+[\mathrm{Im}(\ln M^{(\mathbf{k},\mathbf{b})_{nn}})]^2\}, \tag{B4}$$

$$\Omega_I=\frac{1}{N_{kp}}\sum_{\mathbf{k},\mathbf{b}}w_\mathbf{b}\left(N-\sum_{mn}|M^{(\mathbf{k},\mathbf{b})}_{mn}|^2\right) \tag{B5}$$

and

$$\tilde{\Omega}=\frac{1}{N_{kp}}\sum_{\mathbf{k},\mathbf{b}}w_\mathbf{b}\left(\sum_{m\neq n}|M^{(\mathbf{k},\mathbf{b})}_{mn}|^2+\sum_n[\mathrm{Im}(\ln M^{(\mathbf{k},\mathbf{b})}_{nn})+\mathbf{b}\cdot\bar{\mathbf{r}}_n]^2\right), \tag{B6}$$

where $\mathrm{Im}(\ln M^{(\mathbf{k},\mathbf{b})}_{nn})$ signifies the imaginary part.

In order to calculate the gradient of the spread functional within the space of unitary transformations, we consider the first-order change of Ω by an infinitesimal unitary transformation $U^{(\mathbf{k})}_{mn}=\delta_{mn}+dW^{(\mathbf{k})}_{mn}$. dW is an infinitesimal antiunitary matrix, $dW^\dagger=-dW$. We define

$$R^{(\mathbf{k},\mathbf{b})}_{mn}=M^{(\mathbf{k},\mathbf{b})}_{mn}M^{(\mathbf{k},\mathbf{b})*}_{nn} \tag{B7}$$

and

$$T^{(\mathbf{k},\mathbf{b})}_{mn}=\frac{M^{(\mathbf{k},\mathbf{b})}_{mn}}{M^{(\mathbf{k},\mathbf{b})}_{nn}}\cdot(\mathrm{Im}\ln M^{(\mathbf{k},\mathbf{b})}_{nn}+\mathbf{b}\cdot\bar{\mathbf{r}}_n). \tag{B8}$$

Then,

$$\frac{d\Omega}{dW^{(\mathbf{k})}}=4\sum_\mathbf{b}w_\mathbf{b}[A(R^{(\mathbf{k},\mathbf{b})})-S(T^{(\mathbf{k},\mathbf{b})})], \tag{B9}$$

where $A(R^{(\mathbf{k},\mathbf{b})})=(R^{(\mathbf{k},\mathbf{b})}-R^{(\mathbf{k},\mathbf{b})\dagger})/2$ and $S(T^{(\mathbf{k},\mathbf{b})})=(T^{(\mathbf{k},\mathbf{b})}+T^{(\mathbf{k},\mathbf{b})\dagger})/2i$.

In order to minimize Ω based on the steepest descent method, we first calculate the overlap matrices with periodic parts of initial Bloch functions [see Eq. (44)], $\mathbf{h}^{(I)}_{n\mathbf{k}}(\mathbf{r})=e^{-i\mathbf{k}\cdot\mathbf{r}}\mathbf{H}^{(I)}_{n\mathbf{k}}(\mathbf{r})$,

$$M^{(0)(\mathbf{k},\mathbf{b})}_{mn}=\langle\mathbf{h}^{(I)}_{m\mathbf{k}}|\mathbf{h}^{(I)}_{n\mathbf{k}+\mathbf{b}}\rangle. \tag{B10}$$

We update wave functions as

$$|\mathbf{h}_{n\mathbf{k}}\rangle=\sum_{m=1}^{N}U^{(\mathbf{k})}_{mn}|\mathbf{h}^{(I)}_{m\mathbf{k}}\rangle. \tag{B11}$$

The initial unitary matrix is chosen as $U^{(\mathbf{k})}_{mn}=\delta_{mn}$. We define

$$\Delta W^{(\mathbf{k})} = \frac{\alpha}{4w}\frac{d\Omega}{dW^{(\mathbf{k})}}, \tag{B12}$$

where $w=\Sigma_{\mathbf{b}} w_{\mathbf{b}}$ and we take $\alpha=0.1$ to ensure convergence and numerical stability. Then, the unitary transformation is updated as

$$U^{(\mathbf{k})} \rightarrow U^{(\mathbf{k})} e^{\Delta W^{(\mathbf{k})}}. \tag{B13}$$

Finally, we update the overlap matrices as follows:

$$M^{(\mathbf{k},\mathbf{b})} = U^{(\mathbf{k})\dagger} M^{(0)(\mathbf{k},\mathbf{b})} U^{(\mathbf{k}+\mathbf{b})}. \tag{B14}$$

We repeat the steps from Eq. (B12) to Eq. (B14) until convergence is obtained.

When $N_{\mathbf{k}} > N$, however, we must extract N necessary photonic bands (pseudophotonic bands) from these $N_{\mathbf{k}}$ crossing photonic bands. Then, we must minimize Ω_I before minimizing Ω.

Here, we do not set up an inner frequency window. The stationarity condition $\delta\Omega_I=0$ under the constraint $\langle \mathbf{h}_{m\mathbf{k}} | \mathbf{h}_{n\mathbf{k}} \rangle = \delta_{mn}$, yields the eigenvalue equation,

$$\left(\sum_{\mathbf{b}} w_{\mathbf{b}} P_{\mathbf{k}+\mathbf{b}} \right) | \mathbf{h}_{n\mathbf{k}} \rangle = \lambda_{n\mathbf{k}} | \mathbf{h}_{n\mathbf{k}} \rangle, \tag{B15}$$

where $P_{\mathbf{k}} = \Sigma_{n=1}^{N} | \mathbf{h}_{n\mathbf{k}} \rangle \langle \mathbf{h}_{n\mathbf{k}} |$. The invariant part of the spread functional can then be expressed in terms of the eigenvalue $\lambda_{n\mathbf{k}}$ as

$$\Omega_I = \frac{1}{N_{kp}} \sum_{\mathbf{k}} \left(N \sum_{\mathbf{b}} w_{\mathbf{b}} - \sum_{n=1}^{N} \lambda_{n\mathbf{k}} \right). \tag{B16}$$

From Eqs. (B15) and (B16), we construct N pseudophotonic bands with largest eigenvalues $\lambda_{n\mathbf{k}}$ in order to minimize Ω_I. At each iteration, labelled by i, of the steepest descent method, $\mathbf{h}_{n\mathbf{k}}(\mathbf{r})$ is expressed by a linear combination of $N_{\mathbf{k}}$ original photonic bands $\mathbf{h}^{(0)}_{n\mathbf{k}}(\mathbf{r})$ through a set of coefficients $C^{(i)}_{qn}(\mathbf{k})$ $(q=1,\ldots,N_{\mathbf{k}})$. Substituting $\mathbf{h}^{(i)}_{n\mathbf{k}}(\mathbf{r}) = \Sigma_{q=1}^{N_{\mathbf{k}}} C^{(i)}_{qn}(\mathbf{k}) \mathbf{h}^{(0)}_{q\mathbf{k}}(\mathbf{r})$ into Eq. (B15) on the ith iteration, we obtain

$$\sum_{p=1}^{\mathbf{N_k}} \sum_{q=1}^{\mathbf{N_k}} C^{(i)\dagger}_{mp}(\mathbf{k}) Z^{(i)}_{pq}(\mathbf{k}) C^{(i)}_{qn}(\mathbf{k}) = \lambda_{n\mathbf{k}} \delta_{mn}, \tag{B17}$$

where

$$Z^{(i)}_{pq}(\mathbf{k}) = \langle \mathbf{h}^{(0)}_{p\mathbf{k}} | \sum_{\mathbf{b}} w_{\mathbf{b}} (P^{(i)}_{\mathbf{k}+\mathbf{b}})_{in} | \mathbf{h}^{(0)}_{q\mathbf{k}} \rangle. \tag{B18}$$

Here $(P^{(i)}_{\mathbf{k}+\mathbf{b}})_{\text{in}} = \alpha P^{(i-1)}_{\mathbf{k}+\mathbf{b}} + (1-\alpha)(P^{(i-1)}_{\mathbf{k}+\mathbf{b}})_{\text{in}}$, where $(P^{(0)}_{\mathbf{k}+\mathbf{b}})_{\text{in}} = P^{(0)}_{\mathbf{k}+\mathbf{b}}$ and $\alpha=0.5$ is used to assist numerical stability.[28] We find $N_{\mathbf{k}} \times N_{\mathbf{k}}$ matrix $C^{(i)}(\mathbf{k})$ to diagonalize $N_{\mathbf{k}} \times N_{\mathbf{k}}$ matrix $Z^{(i)}(\mathbf{k})$. Then, we choose N eigenvectors $\mathbf{h}^{(i)}_{n\mathbf{k}}(\mathbf{r})$ with largest eigenvalues and update $(P^{(i+1)}_{\mathbf{k}+\mathbf{b}})_{\text{in}}$ and $P^{(i)}_{\mathbf{k}+\mathbf{b}} = \Sigma_{n=1}^{N} | \mathbf{h}^{(i)}_{n\mathbf{k}+\mathbf{b}} \rangle \langle \mathbf{h}^{(i)}_{n\mathbf{k}+\mathbf{b}} |$. We repeat this iteration until convergence is obtained. We define the resulting, converged N eigvenvectors as the N pseudophotonic bands. Prior to the iterative calculations, we must set up initial Bloch functions $\mathbf{h}^{(I)}_{n\mathbf{k}}(\mathbf{r})$ to obtain $P^{(0)}_{\mathbf{k}+\mathbf{b}} = \Sigma_{n=1}^{N} | \mathbf{h}^{(I)}_{n\mathbf{k}+\mathbf{b}} \rangle \langle \mathbf{h}^{(I)}_{n\mathbf{k}+\mathbf{b}} |$. We project $\mathbf{g}_n(\mathbf{r})$ onto $N_{\mathbf{k}}$ Bloch functions at each $\mathbf{k}$ point and orthonormalize them, according to Eqs. (43) and (44). Details of this procedure are almost identical to that used for MLWF's in electronic band structures.[28]

APPENDIX C: CONSTRUCTING SYMMETRIC FIELD MODES AT DEGENERATE Γ POINT

As shown in Figs. 8, 13, and 18, for both bulk 3D PBG structures and 2D-3D PBG heterostructures, twofold degeneracy appears at the Γ point ($\mathbf{k}=0$) in photonic band structures. Although Γ-point distributions can be chosen to be symmetric in symmetric structures, numerical solutions may yield modes of the form, $\mathbf{h}^{(0)}_{n\mathbf{0}}(\mathbf{r}) = c_1 e^{i\phi_1} \mathbf{f}_1(\mathbf{r}) + c_2 e^{i\phi_2} \mathbf{f}_2(\mathbf{r})$, where ϕ_i are arbitrary phases, c_i are real positive coefficients $(c_1^2 + c_2^2 = 1)$, and $\mathbf{f}_i(\mathbf{r})$ are real symmetric distributions. In structures with mirror symmetries, $\mathbf{f}_i(\mathbf{r})$ are symmetric or antisymmetric with respect to the mirror plane.

The magnetic field at the Γ point is

$$\mathbf{h}^{(0)}_{n\mathbf{0}}(\mathbf{r}) = \sum_{\mathbf{G}} [h^{(0)}_{1,n\mathbf{0}}(\mathbf{G}) \mathbf{e}_1(\mathbf{G}) + h^{(0)}_{2,n\mathbf{0}}(\mathbf{G}) \mathbf{e}_2(\mathbf{G})] e^{i\mathbf{G}\cdot\mathbf{r}}, \tag{C1}$$

where $h^{(0)}_{i,n\mathbf{0}}$ and $\mathbf{e}_i(\mathbf{G})$ $(i=1,2)$ are plane wave expansion coefficients and orthonormal polarization vectors [with $\mathbf{e}_i(\mathbf{G}) \cdot \mathbf{G} = 0$], respectively. We choose

$$\mathbf{e}_1(\mathbf{G}) = (-G_x G_z, -G_y G_z, G_x^2 + G_y^2)/|\mathbf{G}_{\parallel}||\mathbf{G}| \tag{C2}$$

and

$$\mathbf{e}_2(\mathbf{G}) = (G_y, -G_x, 0)/|\mathbf{G}_{\parallel}|, \tag{C3}$$

where $\mathbf{G}_{\parallel} = (G_x, G_y, 0)$. To break the Γ-point degeneracy, when calculating the photonic band structures at the Γ point, we solve the following modified matrix equation:

$$\sum_{\mathbf{G}'} \epsilon^{-1}(\mathbf{G}-\mathbf{G}')|\mathbf{G}||\mathbf{G}'| \times \begin{bmatrix} \mathbf{e}_2(\mathbf{G}) \cdot \mathbf{e}_2(\mathbf{G}') & -\mathbf{e}_2(\mathbf{G}) \cdot \mathbf{e}_1(\mathbf{G}') \\ -\mathbf{e}_1(\mathbf{G}) \cdot \mathbf{e}_2(\mathbf{G}') & \mathbf{e}_1(\mathbf{G}) \cdot \mathbf{e}_1(\mathbf{G}') + e \end{bmatrix} \times \begin{bmatrix} h^{(0)}_{1,n\mathbf{0}}(\mathbf{G}') \\ h^{(0)}_{2,n\mathbf{0}}(\mathbf{G}') \end{bmatrix} = \frac{\omega^2}{c^2} \begin{bmatrix} h^{(0)}_{1,n\mathbf{0}}(\mathbf{G}) \\ h^{(0)}_{2,n\mathbf{0}}(\mathbf{G}) \end{bmatrix}. \tag{C4}$$

The small perturbation $e=10^{-4}$ to the (2,2) diagonal element results in lifting of the double degeneracy and disentangling of the symmetric mode profiles $\mathbf{f}_1(\mathbf{r})$ and $\mathbf{f}_2(\mathbf{r})$.

APPENDIX D: DETERMINATION OF POLARIZATION VECTORS OF THE FIRST AND SECOND Γ-POINT DISTRIBUTIONS

1. Bulk 3D PBG structures

In bulk 3D PBG structures, the first and second Γ-point distributions have an arbitrariness of polarization vectors at $\mathbf{k}=\mathbf{0}$ and $\omega a/2\pi c = 0$. In Eq. (43), $A_{mn} = \langle \mathbf{H}^{(0)}_{m\mathbf{k}} | \mathbf{g}_n \rangle = \Sigma_{\mathbf{G}} A_{mn}(\mathbf{G})$, where $A_{mn}(\mathbf{G}) = \langle \mathbf{h}^{(0)}_{m\mathbf{k}}(\mathbf{G}) \exp[i(\mathbf{k}+\mathbf{G})\cdot\mathbf{r}] | \mathbf{h}^{(0)}_{n\mathbf{0}}(\mathbf{r}) \exp[-(\mathbf{r}-\mathbf{r}^{(n)})^2/\sigma^2] \rangle$. The first and second Γ-point distributions are uniform. However, when fixing the polarization vectors of these distributions,

$\mathbf{H}^{(0)}_{m\mathbf{k}}(\mathbf{r})$ and $\mathbf{g}_n(\mathbf{r})$ become orthogonal at a certain $\mathbf{k}$ point. This causes the error in the calculation of $S^{-1/2}$ in Eq. (44). To prevent this error, $\mathbf{h}^{(0)}_{n\mathbf{0}}(\mathbf{r})$ $(n=1,2)$ are assumed to depend on $\mathbf{k}+\mathbf{G}$ of $\mathbf{H}^{(0)}_{m\mathbf{k}}(\mathbf{r})$ in the calculation of $A_{mn}(\mathbf{G})$. In this case, we define $\mathbf{q}=\mathbf{k}+\mathbf{G}$ and polarizations of the first and second Γ-point distributions as follows:

$$\mathbf{e}_1(\mathbf{k}+\mathbf{G}) = (-q_x q_z, -q_y q_z, q_x^2+q_y^2)/|\mathbf{q}_\parallel||\mathbf{q}|, \tag{D1}$$

$$\mathbf{e}_2(\mathbf{k}+\mathbf{G}) = i(q_y, -q_x, 0)/|\mathbf{q}_\parallel|, \tag{D2}$$

where $\mathbf{q}_\parallel=(q_x,q_y,0)$. $\mathbf{e}_2(\mathbf{k}+\mathbf{G})$ is fixed in the 2D plane. $|\mathbf{e}_1(\mathbf{k}+\mathbf{G})|=|\mathbf{e}_2(\mathbf{k}+\mathbf{G})|=1$, and $\mathbf{e}_1(\mathbf{k}+\mathbf{G})$, $\mathbf{e}_2(\mathbf{k}+\mathbf{G})$ and $\mathbf{k}+\mathbf{G}$ are orthonormal. $\mathbf{e}_2(\mathbf{k}+\mathbf{G})$ is pure imaginary so that the initial Bloch function satisfies $\mathbf{H}^{(I)}_{2\mathbf{k}}(\mathbf{r})=\mathbf{H}^{(I)*}_{2-\mathbf{k}}(\mathbf{r})$. Then,

$$A_{m1}(\mathbf{G}) = \langle \mathbf{h}^{(0)}_{m\mathbf{k}}(\mathbf{G}) \exp[i(\mathbf{k}+\mathbf{G})\cdot\mathbf{r}] | \mathbf{e}_1(\mathbf{k}+\mathbf{G}) \times \exp[-(\mathbf{r}-\mathbf{r}^{(n)})^2/\sigma^2] \rangle$$

and

$$A_{m2}(\mathbf{G}) = \langle \mathbf{h}^{(0)}_{m\mathbf{k}}(\mathbf{G}) \exp[i(\mathbf{k}+\mathbf{G})\cdot\mathbf{r}] | \mathbf{e}_2(\mathbf{k}+\mathbf{G}) \times \exp[-(\mathbf{r}-\mathbf{r}^{(n)})^2/\sigma^2] \rangle.$$

2. 2D-3D PBG heterostructures

Similarly, in 2D-3D PBG heterostructures, the first and second Γ-point distributions have an arbitrariness of polarization vectors at $\mathbf{k}_\parallel=\mathbf{0}_\parallel$ and $\omega a/2\pi c=0$. In Eq. (72), $A_{mn}=\Sigma_{\mathbf{G}_\parallel}\Sigma_{G_z}A_{mn}(\mathbf{G}_\parallel,G_z)$, where

$$A_{mn}(\mathbf{G}_\parallel,G_z) = \langle \mathbf{h}^{(0)}_{m\mathbf{k}_\parallel}(\mathbf{G}_\parallel,G_z) \exp\{i[(\mathbf{k}_\parallel+\mathbf{G}_\parallel)\cdot\mathbf{r}_\parallel + G_z z]\} | \mathbf{h}^{(0)}_{n\mathbf{0}_\parallel}(\mathbf{r}_\parallel,z) \exp[-(\mathbf{r}_\parallel-\mathbf{r}^{(n)}_\parallel)^2/\sigma^2] \rangle.$$

In this case, we define $\mathbf{q}_\parallel=\mathbf{k}_\parallel+\mathbf{G}_\parallel$ and polarizations of the first and second Γ-point distributions as follows:

$$\mathbf{e}_1(\mathbf{k}_\parallel+\mathbf{G}_\parallel) = (0,0,1) \tag{D3}$$

$$\mathbf{e}_2(\mathbf{k}_\parallel+\mathbf{G}_\parallel) = i(q_y, -q_x, 0)/|\mathbf{q}_\parallel|, \tag{D4}$$

$\mathbf{e}_2(\mathbf{k}_\parallel+\mathbf{G}_\parallel)$ is fixed in the 2D plane. $|\mathbf{e}_1(\mathbf{k}_\parallel+\mathbf{G}_\parallel)|=|\mathbf{e}_2(\mathbf{k}_\parallel+\mathbf{G}_\parallel)|=1$, and $\mathbf{e}_1(\mathbf{k}_\parallel+\mathbf{G}_\parallel)$, $\mathbf{e}_2(\mathbf{k}_\parallel+\mathbf{G}_\parallel)$ and $\mathbf{k}_\parallel+\mathbf{G}_\parallel$ are orthonormal. $\mathbf{e}_2(\mathbf{k}_\parallel+\mathbf{G}_\parallel)$ is pure imaginary so that the initial Bloch function satisfies $\mathbf{H}^{(I)}_{2\mathbf{k}_\parallel}(\mathbf{r}_\parallel,z)=\mathbf{H}^{(I)*}_{2-\mathbf{k}_\parallel}(\mathbf{r}_\parallel,z)$. Then,

$$A_{m1}(\mathbf{G}_\parallel,G_z) = \langle \mathbf{h}^{(0)}_{m\mathbf{k}_\parallel}(\mathbf{G}_\parallel,G_z) \exp\{i[(\mathbf{k}_\parallel+\mathbf{G}_\parallel)\cdot\mathbf{r}_\parallel + G_z z]\} | \mathbf{e}_1(\mathbf{k}_\parallel+\mathbf{G}_\parallel) \exp[-(\mathbf{r}-\mathbf{r}^{(n)})^2/\sigma^2] \rangle$$

and

$$A_{m2}(\mathbf{G}_\parallel,G_z) = \langle \mathbf{h}^{(0)}_{m\mathbf{k}_\parallel}(\mathbf{G}_\parallel,G_z) \exp\{i[(\mathbf{k}_\parallel+\mathbf{G}_\parallel)\cdot\mathbf{r}_\parallel + G_z z]\} | \mathbf{e}_2(\mathbf{k}_\parallel+\mathbf{G}_\parallel) \exp[-(\mathbf{r}-\mathbf{r}^{(n)})^2/\sigma^2] \rangle.$$

[1] S. John, Phys. Rev. Lett. **58**, 2486 (1987).
[2] E. Yablonovitch, Phys. Rev. Lett. **58**, 2059 (1987).
[3] S. John, Phys. Rev. Lett. **53**, 2169 (1984).
[4] A. Chutinan and S. Noda, Appl. Phys. Lett. **75**, 3739 (1999).
[5] A. Chutinan, S. John, and O. Toader, Phys. Rev. Lett. **90**, 123901 (2003).
[6] A. Chutinan and S. John, Phys. Rev. E **71**, 026605 (2005).
[7] V. Yannopapas, A. Modinos, and N. Stefanou, Phys. Rev. B **65**, 235201 (2002).
[8] E. Lidorikis, M. M. Sigalas, E. N. Economou, and C. M. Soukoulis, Phys. Rev. Lett. **81**, 1405 (1998).
[9] J. P. Albert, C. Jouanin, D. Cassagne, and D. Bertho, Phys. Rev. B **61**, 4381 (2000).
[10] J. P. Albert, C. Jouanin, D. Cassagne, and D. Monge, Opt. Quantum Electron. **34**, 251 (2002).
[11] M. Le Vassor D"yerville, D. Monge, D. Cassagne, and J. P. Albert, Opt. Quantum Electron. **34**, 445 (2002).
[12] K. Busch, S. F. Mingaleev, A. Garcia-Martin, M. Schillinger, and D. Hermann, J. Phys.: Condens. Matter **15**, R1233 (2003).
[13] D. M. Whittaker and M. P. Croucher, Phys. Rev. B **67**, 085204 (2003).
[14] G. H. Wannier, Phys. Rev. **52**, 191 (1937).
[15] N. W. Ashcroft and N. D. Mermin, *Solid State Physics* (Thomson Learning, New York, 1976).
[16] A. Mekis, J. C. Chen, I. Kurland, S. Fan, P. R. Villeneuve, and J. D. Joannopoulos, Phys. Rev. Lett. **77**, 3787 (1996).
[17] A. Mekis, S. Fan, and J. D. Joannopoulos, Phys. Rev. B **58**, 4809 (1998).
[18] M. M. Sigalas, R. Biswas, K. M. Ho, C. M. Soukoulis, D. Turner, B. Vasiliu, S. C. Kothari, and S. Lin, Opt. Technol. **23**, 56 (1999).
[19] S. Fan, P. R. Villeneuve, J. D. Joannopoulos, and H. A. Haus, Phys. Rev. Lett. **80**, 960 (1998).
[20] T. Asano, B. S. Song, Y. Tanaka, and S. Noda, Appl. Phys. Lett. **83**, 407 (2003).
[21] K. M. Ho, C. T. Chan, and C. M. Soukoulis, Phys. Rev. Lett. **65**, 3152 (1990).
[22] K. Busch and S. John, Phys. Rev. E **58**, 3896 (1998).
[23] A. Taflove and S. C. Hagness, *Computational Electrodynamics: The Finite-Difference Time-Domain Method* (Artech House, Boston, 1995).
[24] A. Chutinan and S. John, Phys. Rev. B **72**, 161316(R) (2005).
[25] A. Chutinan and S. John, Opt. Express **14**, 1266 (2006).
[26] M. Deubel, G. von Freymann, and M. Wegener (unpublished).
[27] N. Marzari and D. Vanderbilt, Phys. Rev. B **56**, 12847 (1997).
[28] I. Souza, N. Marzari, and D. Vanderbilt, Phys. Rev. B **65**, 035109

(2001).
[29] S. F. M. Mingaleev and Y. S. Kivshar, J. Opt. Soc. Am. B **19**, 2241 (2002).
[30] A. J. Jerri, *The Gibbs Phenomenon in Fourier Analysis, Splines and Wavelet (Mathematics and Its Applications)*, 1st ed. (Springer, New York, 1998).
[31] K. M. Leung, J. Opt. Soc. Am. B **10**, 303 (1993).
[32] K. M. Ho, C. T. Chan, C. M. Soukoulis, R. Biswas, and M. Sigalas, Solid State Commun. **89**, 413 (1994).
[33] S.-Y. Lin, J. Fleming, D. Hetherington, B. Smith, R. Biswas, K. Ho, M. Sigalas, W. Zubrzycki, S. Kurtz, and J. Bur, Nature (London) **394**, 251 (1998).
[34] S. Noda, K. Tomoda, N. Yamamoto, and A. Chutinan, Science **289**, 604 (2000).